Mo Occupancy Along Crystallographic Shear Planes in the Wadsley–Roth Compound $Mo_xNb_{12}W_{1-x}O_{33}$ Enables Multi-Electron Redox Behavior

Luke D. Salzer,[†,a] *Cami Christensen,*[†,a] *Claire Y. Gervais,*[a] *Alexander G. Squires,*[b] *Alexis G. Manche,*[b] *Danielle R. Lustig,*[a] *Amy L. Prieto,*[a] *James R. Neilson,*[a] *David O. Scanlon,*[b] *Justin B. Sambur*[*,a]

[a]Department of Chemistry, Colorado State University, Fort Collins, CO 80523, USA

[b]School of Chemistry, University of Birmingham, Edgbaston, B15 2TT

*corresponding author

† Authors contributed equally to this work

KEYWORDS.

Energy storage, transition metal oxides, Li-ion diffusivity, structure-property relationships, defects, Wadsley-Roth phases

ABSTRACT.

Transition metal oxide Wadsley-Roth (W-R) crystallographic shear compounds are promising alternatives to graphite for high-rate Li-ion battery applications, as fast charging can drive unsafe lithium metal plating on graphite anodes when Li^+ ions deposit as metallic lithium rather than intercalating into the graphite lattice. Despite this promise, fundamental materials chemistry questions remain regarding how to tune W-R structure and composition to achieve desirable electrochemical properties such as lower working potential, enhanced capacity, and improved cycle stability. Our work is motivated by two central questions: (1) how transition-metal substitution and site occupancy modifies the electrochemically active density of states (DOS) that governs multi-electron redox and the working potential; and (2) how variations in the propensity for second-order Jahn–Teller (SOJT) distortions of transition-metal octahedra along crystallographic shear planes may influence structural stability during repeated cycling. To answer these questions, we systematically investigated a series of nearly phase pure $Mo_xNb_{12}W_{1-x}O_{33}$ and defect-rich D-$Mo_xNb_{12}W_{1-x}O_{33}$ samples, as evidenced by experimental and computational Raman spectroscopy, as well as X-ray diffraction and Rietveld refinement analyses. Galvanostatic cycling and differential capacity measurements revealed that Mo substitution for W alters the electrochemically active DOS and activates multi-electron redox. Mo substitution introduces new electrochemically active states at more positive potentials than the W-based compounds. Electronic structure calculations show that the states enabling multi-electron redox are highly sensitive to both the identity of the transition-metal dopant (W vs. Mo) and its crystallographic site; accordingly, we considered doping at the tetrahedral, block-center, and shear-plane sites, finding that multi-electron ($Mo^{6+} \rightarrow Mo^{4+}$) redox arises specifically from Mo occupying the edge-sharing octahedral sites along the shear planes. The defective samples generally exhibited higher capacities, likely due to the presence of Wadsley defects (e.g., intergrowth of $W_4Nb_{26}O_{77}$ in a

matrix of $Nb_{12}WO_{33}$) that further lower Li-ion binding energetics and alter Li-ion transport paths. Mo-rich samples exhibit greater capacity loss with additional cycling, possibly due to the inability of severely distorted Mo octahedra from “rocking” back and forth during lithiation/de-lithiation cycles. These findings are significant because they inform W-R material design strategies aimed at systematically increasing capacity and working potential via optimizing transition metal site occupancy in the structure.

Introduction.

Transition metal oxide W-R crystallographic shear compounds are promising anode materials that could replace graphite in high-rate Li-ion battery applications. Wadsley, Roth, Allpress, and Anderson first established the structural principles of W-R crystallographic shear structures in the 1960s.[1–8] In 1983, Cava et al. chemically lithiated a series of niobium-based Wadsley–Roth oxides, including titanium-, vanadium-, tungsten-, and germanium-containing compounds.[9] In 2018, Grey and co-workers incorporated W-R $Nb_{16}W_5O_{55}$ materials into fast-charging Li-ion battery electrodes with higher volumetric capacity and superior rate capability compared to traditional graphite anodes.[10] A major advantage of niobium oxide-based W-R anode materials is that they operate outside the potential window where lithium dendrites form, positioning them as safe electrodes for high-rate energy storage applications.[11–16] Despite these advantages and the strong performance metrics demonstrated to date,[10] the growing interest in niobium oxide–based W-R anodes has also clarified several outstanding challenges that must be addressed to fully realize their potential as graphite replacements.[17] First, W-R phases operate at higher average lithiation potentials than graphite, resulting in a nontrivial voltage penalty at the full-cell level. Second, while these materials nominally contain redox-active transition metals, accessing reversible multi-electron redox across all metal sites remains poorly understood. Third, strategies that simultaneously enable multi-electron reduction of the framework while preserving structural integrity and long-term reversibility under high-rate cycling conditions are still lacking.

There has been substantial effort toward defining compositional and structural design rules for W-R anode materials,[18–20] yet a fundamental materials chemistry challenge remains: transition metals in W-R frameworks occupy multiple, crystallographically distinct sites rather than a single uniform environment.[21–23] W-R phases are built from $n \times m$ blocks of corner-sharing MO_6 octahedra separated by crystallographic shear planes composed of edge-sharing octahedra, with additional tetrahedral sites at block corners that fill structural voids (Figure 1).[1,24] This intrinsic structural heterogeneity complicates efforts to rationally tune electrochemical properties, as not all metal sites are expected to contribute equally to reversible redox under practical operating conditions.

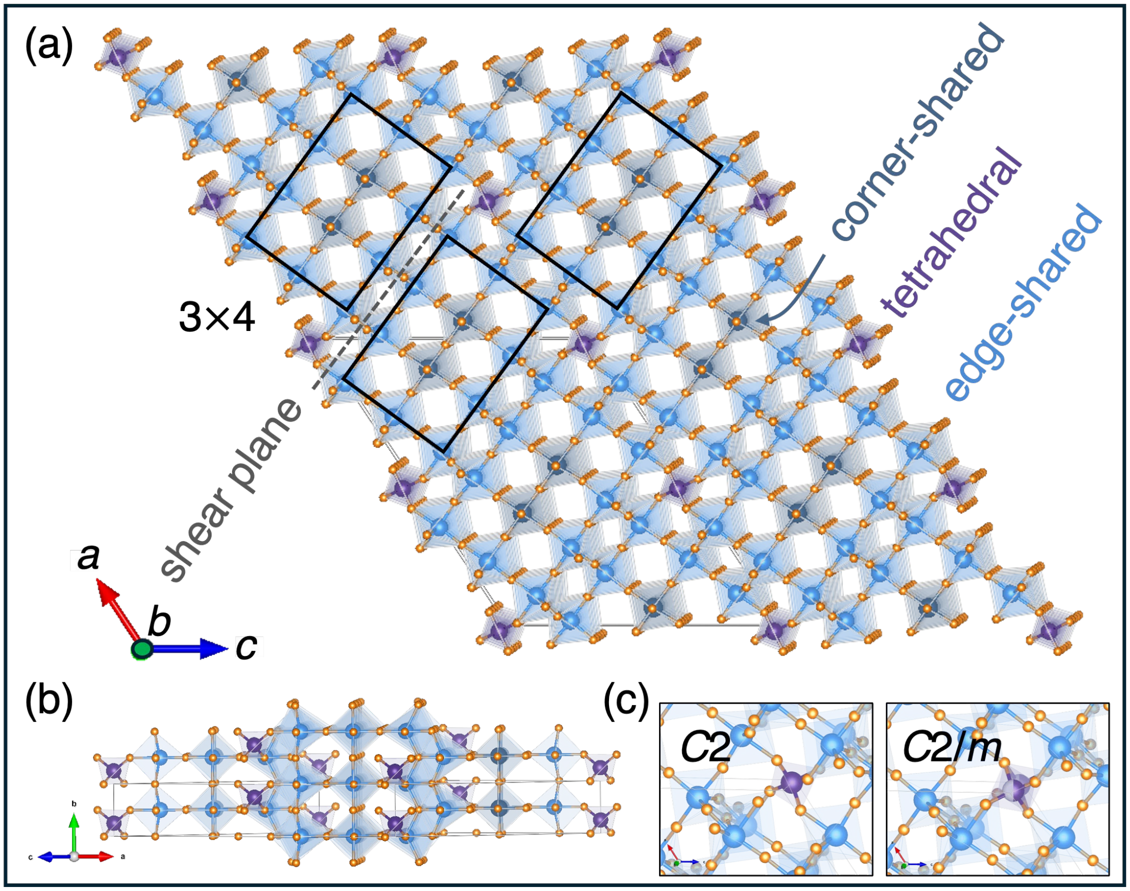

Figure 1. (a) Illustration of the crystal structure of $Mo_xNb_{12}W_{1-x}O_{33}$ ($C2$ symmetry) highlighting the 3×4 octahedral blocks, shear planes, corner-sharing octahedra (dark blue), edge-shared octahedra (light blue), and tetrahedra (purple). (b) Alternative orientation of $Mo_xNb_{12}W_{1-x}O_{33}$ orthogonal to the 3×4 blocks. (c) Illustration of the tetrahedrally ordered $C2$ vs tetrahedrally disordered $C2/m$ crystal structures.

One strategy for addressing cation disorder in W-R materials is to focus on systems in which elemental substitution is strongly biased toward a specific crystallographic site. For example, Preefer et al. proposed that redox-active V preferentially substitutes for P at the tetrahedral site in PNb_9O_{25},[25] providing a platform to examine how site-specific substitution influences electrochemical behavior. The authors synthesized the isostructural (3×3) compounds PNb_9O_{25} and VNb_9O_{25} and demonstrated that, under slow charge–discharge conditions, they can reversibly store approximately 11 and 14 electrons (and Li^+ ions) per formula unit, respectively. Substituting

V or P increased the number of Nb centers participating in multi-electron redox (Nb^{5+} → Nb^{3+}). Ex situ X-ray photoelectron spectroscopy indicated that P remained redox-inactive during cycling, while V contributed partially to charge storage, suggesting that V redox alone could not account for the enhanced capacity. When the charge–discharge rate was increased by an order of magnitude, the capacity of VNb_9O_{25} decreased substantially to ~9 electrons per formula unit, whereas PNb_9O_{25} largely retained its initial capacity of ~11 electrons per formula unit. Similar rate-dependent suppression of multi-electron redox has been reported across a range of W-R and related shear oxides, including Nb-O, W-Nb-O, Ti-Nb-O, P-Nb-O, Mo-Nb-O versus Ta-Nb-O, and V-Nb-O.[10,19,25–31] Collectively, these observations underscore the sensitivity of multi-electron redox to both cation identity and crystallographic site occupancy, highlighting the need for fundamental studies that link structure, site-specific chemistry, and rate-dependent electrochemical performance.

In parallel, increasing attention has been directed toward elemental substitution along the crystallographic shear planes. Recent first-principles electronic structure calculations by Saber et al. revealed an unconventional redox mechanism upon Li-ion insertion in the $Li_xTiNb_2O_7$ W-R phase that results in the formation of metal−metal bonds between Nb octahedra along the shear plane.[32] This metal dimer redox mechanism significantly impacts the structure by shortening cation-pair distances, which subsequently affects the lattice parameters of the host, and can impact Li-ion site preferences as the Li concentration changes. An interesting open question is to what extent metal-metal bonding occurs in niobium tungsten oxide W-R phases. In this work, we chose to study Mo substitution for W because metal-metal bonding has been reported in molybdenum oxides such as $LiScMo_3O_8$[33] and Mo exhibits greater SOJT distortion effects than W.[23,34]

In particular, $MoNb_{12}O_{33}$ and $WNb_{12}O_{33}$ W-R oxides have attracted significant attention for their exceptional rate capability and multi-electron redox behavior as lithium-ion battery anodes. In 2019, Zhu et al. reported multi-electron $Mo^{6+} \rightarrow Mo^{4+}$ reduction in micron-sized $MoNb_{12}O_{33}$ spheres and remarked that all Mo^{6+} occupies the tetrahedral site.[35] The materials exhibited 5% capacity loss after 100 cycles at 1C rates. Yang et al. synthesized $MoNb_{12}O_{33}$ microspheres via a hydrothermal method and reported high practical capacity (298 mA h g^{-1} at 0.5 C), superior rate capability (168 mA h g^{-1} at 20 C), and excellent cyclability (capacity retention of 90 % over 500 cycles at 10 C).[36] Additionally, Deng et al. reported that nanostructuring $MoNb_{12}O_{33}$ into a sheet-like structure with abundant holes further enhances performance.[37] Electrochemical studies of $MoNb_{12}O_{33}$ anodes in NMC622||$MoNb_{12}O_{33}$ full cells have shown unusually fast lithium-ion insertion kinetics and high rate capability.[38] Notably, these cells sustain rapid charging at low temperatures, retaining substantial capacity even at 0 °C. Our group investigated how the block structure influences Li-ion diffusivity, capacity, and cycle stability in 3×4 $Nb_{12}WO_{33}$, 4×4 $Nb_{14}W_3O_{44}$, and 4×5 $Nb_{16}W_5O_{55}$.[39] Li-ion diffusivity increased with block size, in agreement with theoretical predictions,[27,40,41] and the 4×4 $Nb_{14}W_3O_{44}$ compound exhibited higher capacity and reversibility than the 3×4 $Nb_{12}WO_{33}$ and 4×5 $Nb_{16}W_5O_{55}$. Despite these extensive electrochemical studies, a clear mechanistic understanding of how Mo substitution for W alters the electrochemically active density of states governing multi-electron redox is lacking.

One final consideration is that Wadsley defect phases, which can involve the intergrowth of another W-R phase within the matrix of another (e.g., $W_4Nb_{26}O_{77}$ in a matrix of $Nb_{12}WO_{33}$),[42] commonly emerge during synthesis. Wadsley defects complicate attempts to unambiguously assign observed functional properties to intentional compositional modifications, rather than unintended structural disorder. Subtle differences in experimental conditions can lead to the formation of defect phases,[43] which are not easily identifiable by powder X-ray diffraction (PXRD). These defects can enhance specific capacity, rate capability, and stability, as seen in the crystallographic shear compound H-Nb_2O_5.[44–46] It is unclear how different synthetic procedures (e.g., high-temperature solid-state synthesis, hydrothermal growth, sol-gel growth, or microwave synthesis[39,47,48]) influence material crystallinity and purity that ultimately determine the materials' functional properties. This raises the question: how does the community determine if a performance increase in W-R materials is due to intended structure or doping changes, or an unintended minor impurity phase?

In this work, we systematically investigated $Mo_xNb_{12}W_{1-x}O_{33}$ compounds synthesized via high temperature solid-state reactions with different reaction conditions to deconvolute elemental substitution versus phase purity effects on electrochemical performance. Notably, we discovered that substituting Mo for W activates multi-electron redox behavior specifically when Mo occupies the edge-sharing octahedral sites along the crystallographic shear planes. However, the enhanced capacity observed in Mo-rich compounds is often coupled to diminished cycling stability, highlighting a fundamental trade-off that remains poorly understood. We attribute the electrochemical irreversibility to the inability of severely distorted octahedra on the shear plane from "rocking" back and forth during lithiation/de-lithiation cycles. Disordered samples also exhibit greater capacity, likely due to the presence of Wadsley defects that lower Li-ion binding energetics.[46]

Experimental Methods.

Synthesis of Nearly Phase Pure W-R compounds. Five $Mo_xNb_{12}W_{1-x}O_{33}$ (x = 0.00, 0.25, 0.50, 0.75, 1.00) samples were synthesized by first grinding stoichiometric ratios (12:1:0, 48:3:1, 24:1:1, 48:1:3, 12:0:1) of NbO_2 (Alfa Aesar, 99%), $WO_{2.9}$ (Alfa Aesar, 99%), and MoO_3 (Thermo Scientific, 99%), respectively, using an agate mortar and pestle in air. In this work, x is defined by the molar ratio of starting precursors. The ground mixtures were pressed into pellets with a hydraulic press (Caver Model: 4350.L) using 2 tons of pressure. The $x = 0.00$, 0.25, and 0.50 pellets were heated in a Thermo Scientific Lindberg Blue M tube furnace in air from room temperature to 1200 °C at a rate of 1 °C min^{-1}, held at 1200 °C for 12 hours, and then cooled to room temperature at a rate of 1 °C min^{-1}. The setpoint temperature and ramp rates were adapted from literature.[10,39] The $x = 0.75$ and 1.0 pellets were heated in air from room temperature to 900 °C, held at 900 °C for 12 hours, and then cooled to room temperature at a rate of 10 °C min^{-1}, following literature.[49]

<u>Synthesis of Defect-Rich W-R Compounds</u>. Four defect-rich samples, denoted as D-$Mo_xNb_{12}W_{1-x}O_{33}$ compounds (x = 0.00, 0.25, 0.75, 1.00), were synthesized by grinding stoichiometric ratios (12:1:0, 48:3:1, 48:1:3, 12:0:1) of NbO_2, $WO_{2.9}$, and MoO_3, respectively, using an agate mortar and pestle in air . The ground mixtures were pressed into pellets with a hydraulic press at 2 tons of pressure. The $x = 0.0$ and 0.25 pellets were heated in air in the same tube furnace from room temperature (~20°C) to 1200 °C at a rate of 10 °C min^{-1}, held at 1200 °C for one minute, and then cooled to room temperature at a rate of 10°C min^{-1}. The $x = 0.75$ and 1.0 samples were heated in air from room temperature to 900 °C, held at 900 °C for one minute, and then cooled to room temperature at a rate of 10°C min^{-1}.

<u>Materials Characterization</u>. The crystal structures of the compounds were characterized by powder x-ray diffraction (PXRD) using a Bruker D8 Discover DaVinci – Powder Diffractometer (Cu Kα radiation). Scanning electron microscopy (SEM) images were collected using a JEOL JSM-6500 field emission scanning electron microscope operating at a 15 keV accelerating

voltage and a working distance of 10 mm. Raman spectroscopy was performed on an Olympus IX-73 inverted optical microscope with either a Oxxius 532 nm SLM DPSS or a 785 nm Oxxius SA LBX-785HPE laser source. A 20× NA0.95 air objective (Olympus PlanFL N20X) focused the laser source onto the sample, which was prepared by placing the powered sample on a quartz microscope slide. Raman signals were collected in a backscatter geometry by passing the photons to a Horiba iHR550 spectrometer (1200 gr/mm), which was used to disperse the Raman signal on a Horiba Synapse back-illuminated deep depletion charge coupled device (CCD) camera for detection. The Raman spectrometer wavenumber axis was calibrated using the Stokes and anti-Stokes peaks of a Si standard sample at -521 cm^{-1} and 521 cm^{-1}, respectively. All Raman spectra were acquired under the same conditions at room temperature.

Simulated diffraction patterns were generated with VESTA using the originally-reported $Nb_{12}WO_{33}$ crystal structure (ICSD coll. Code 23799, Ref [50]). Redefining the structure from *C*2 to *C*2/*m* keeps the multiplicity of all atoms the same, except for W, and provides a better description of the data. The increase in symmetry provides an additional tetrahedrally-coordinated W site; its occupancy is then set to 0.5 to retain the overall composition. This *C*2/*m* structure is then used for the analysis at each for each composition.

Vienna Ab initio Simulation Package (VASP) Calculations. Electronic structure calculations using VASP were carried out using the projector-augmented wave method.[51,52] Plane-wave energy cutoffs of 650 eV were used along with a minimum k-point spacing of 0.3 A^{-1}. The pseudopotentials used were Nb_sv, Mo_sv, O and W_sv. Energies during electronic minimization had a convergence tolerance of 10^{-6}, and forces during structural relaxation were deemed converged when they fell below -0.01 eV/Å on all atoms in the calculation. Calculations used either the GGA functional PBEsol[53] or the R2SCAN metaGGA functional.[54] The functional used for each calculation is indicated in the main text. Pre-and post-processing used the pymatgen,[55] numpy,[56] doped,[57] ase,[58] icet[59] and bsym[60] packages.

Raman Calculations. Periodic Raman calculations were carried out with CRYSTAL23,[61] using analytical Γ-point phonons and Raman tensors within the coupled-perturbed Kohn–Sham (CPKS) framework.[62] Raman calculations were performed on ordered structural models derived from the Wadsley–Roth framework, with Mo or W placed on specific tetrahedral, corner-sharing octahedral, or shear-plane edge-sharing octahedral sites; these ordered models were used in place of the fractional split-site *C*2/*m* Rietveld model, which is not amenable to periodic DFT calculations. To obtain reliable Raman activities (polarizability derivatives) in these d-electron oxides, we employed a PBEsol-based global hybrid constructed by mixing 25% exact (Hartree–Fock) exchange with PBEsol exchange and using PBEsol correlation (PBEsol0-type).[53,63,64] PBEsol was selected as the semilocal base because it improves equilibrium properties of densely packed solids, which impacts vibrational frequencies, while inclusion of exact exchange mitigates over-delocalization/self-interaction effects that can influence the electronic response underlying Raman intensities. All calculations used spin polarization and the pob-TZVP-rev2 all-electron Gaussian basis sets for Nb, Mo, W, and O.[65,66] A representative input for $MoNb_{12}O_{33}$ used a 184-atom supercell; the full input deck is provided in the Supporting Information. Brillouin-zone sampling and integral thresholds were converged such that all Γ-point frequencies and Raman activities changed by <5 cm^{-1} and <5% upon further tightening. In practice, a k-point grid equivalent to 2×6×3 for response properties and sufficient convergence in total energies and spin densities was obtained by application of integral series truncation thresholds of 10^{-7}, 10^{-7}, 10^{-7}, 10^{-7}, and 10^{-14} for Coulomb overlap and penetration, exchange overlap, and g- and n-series exchange penetration, respectively, were sufficient for the large cells considered in the CRYSTAL23 documentation.

SCF convergence employed direct inversion with level shifting and Fermi–Dirac mixing to ensure stable hybrid iterations. Raman activities were converted to observable intensities using CRYSTAL's experimental formalism at 300 K and the experimental laser line (785 nm) used in this study, followed by Lorentzian broadening (FWHM 10–12 cm^{-1}) to mimic instrument response.[61,62,67]

Normal-mode analysis was carried out with phonopy (v2.28.0).[68] The vibrational step used the VASP-relaxed C2/m structures as starting geometries; Γ-point eigenvectors from CRYSTAL23 were used for Raman assignments and compared across models by frequency proximity and maximized normalized eigenvector overlap to ensure consistent tracking of corresponding modes between site-occupancy configurations. We used phonopy for the mode analysis because it provides a code-agnostic post-processing layer with consistent eigenvector normalization and symmetry handling.

Coin Cell Construction. Coin cell batteries were constructed in an argon glove box using the following components: stainless steel cases (MTI Corp, CR2032), a stainless-steel wave spring (MTI Corp, CR20WS), a stainless-steel spacer (MTI Corp, CR20-Spacer-05), and a glass microfiber (VWR, 691) separator. The metal oxide composite electrode was prepared by grinding an 8:1:1 ratio of W-R particles, conductive carbon (Super P, Alfa Aesar), and polyvinylidene fluoride binder (PVDF, Sigma Aldrich) in an agate mortar and pestle. The metal oxide composite electrode is the cathode and lithium metal is the anode in this coin cell geometry. This mixture was dispersed in N-methyl pyrrolidone (NMP, Sigma-Aldrich) until the solution was slightly viscous. A doctor blade was used to cast a 100 μm-thick film onto a copper substrate. The film was dried overnight in vacuum at 150 °C. The dried film was punched into several ½ inch electrodes and transferred into an argon glove box. Coin cells were constructed with the MTI coin cell case using a ½ inch diameter lithium metal electrode and a 5/8th inch diameter separator with 80.0 µL of electrolyte containing 1M $LiPF_6$ dissolved in a 1:1 volume ratio of ethylene carbonate/dimethyl carbonate (EC/DMC, Sigma Aldrich) was pipetted onto the separator. The cathode was placed on the separator after it had become saturated with electrolyte, followed by the stainless-steel spacer, spring, and finally the end cap. The cells were pressed with 0.9 tons of pressure using a compact digital pressure controlled electric crimper (MTI MSK-160E). The cells rested for 12 h before electrochemical measurements were performed to allow the electrolyte to fully saturate the separator. Data in this study stems from 3 coin cells for $Nb_{12}WO_{33}$, $Mo_{0.25}Nb_{12}W_{0.75}O_{33}$, $Mo_{0.5}Nb_{12}W_{0.5}O_{33}$, $Mo_{0.75}$ $Nb_{12}W_{0.25}O_{33}$, and $MoNb_{12}O_{33}$ and $N = 4$, 2, 3, and 4 coin cells for D-$Nb_{12}WO_{33}$, D- $Mo_{0.25}Nb_{12}W_{0.75}O_{33}$, $Mo_{0.75}$ $Nb_{12}W_{0.25}O_{33}$, and D-$MoNb_{12}O_{33}$, respectively.

Electrochemical Testing. The coin cells were cycled on an Arbin battery tester (LBT-20084) at a C-rate of C/3. The C-rate is the current value required to fully charge/discharge the active material in the electrode, expressed as a multiple of its theoretical capacity. The theoretical capacity is calculated according to $Q_{theoretical} = nF/3.6M$, where n is the number of electrons transferred per formula unit, F is Faraday's constant, 3.6 is a conversion factor between coulombs and mAh/g, and M is the molecular weight. The C-rate was calculated according to following equation: $I = (Q_{theoretical} \times m)/t$, where I is the current applied, m is the mass of active material, and t is time in hours.

Results

Composition and Structural Analysis. We synthesized two series of $Mo_xNb_{12}W_{1-x}O_{33}$ W-R samples using different reaction conditions to deconvolute how intentional chemical substitution effects (i.e., Mo for W) influences electrochemical properties as opposed to unintentional morphology, crystallinity, and/or phase impurity contributions to the electrochemical properties. Researchers typically synthesize niobium tungsten oxide W-R compounds at high temperatures (>900°C) for long times (>12 h), but it remains unclear how specific reaction temperature and time conditions influence the product phase purity and electrochemical cycling behavior in Li-ion containing electrolytes.[10,39,47,69,70] We hypothesize that maintaining high reaction temperatures for long times promotes the formation of phase pure products and minimizes defect formation, such as Wadsley defects or other intergrowths that will be discussed in more detail below.[7,27,46] To test this hypothesis, we synthesized two different Mo-substituted W-R samples using the same precursors but different reaction conditions. To do so, we hand-ground stoichiometric ratios of NbO_2, $WO_{2.9}$, and MoO_3 in a mortar and pestle, pressed the powder into a pellet, and heated both samples to the same setpoint temperature, but with different ramp rates and setpoint temperature hold times. One reaction condition involved slowly heating (1 °C min^{-1}) the sample to the setpoint temperature and maintaining that temperature for 12 h. The other reaction condition involved rapid heating (10 °C min^{-1}) and maintaining the set point temperature for only 1 min.

Figure 2 compares background subtracted experimental PXRD patterns for the $Mo_xNb_{12}W_{1-x}O_{33}$ compounds that were slowly heated and maintained at the setpoint temperature for 12 h to model diffraction patterns for $Nb_{12}WO_{33}$ (CIF collection code 23799, *C*2 space group) and $MoNb_{12}WO_{33}$ (*C*2 space group). We observe quantitative agreement with the reported structures (Figure S1), with improved agreement by increasing the space group symmetry to *C*2/*m* and putting the tetrahedral W/Mo site at split site occupancy (=0.5; this is the only site multiplicity that changes upon changing the space group). No residual NbO_2, $WO_{2.9}$, and MoO_3 starting materials remain after synthesis. There is no systematic shift in lattice parameters with increasing x in the nonlithiated structures. Across the Mo substitution series, the quantitative phase analysis follows the systematic substitution levels on the tetrahedral "corner" site. As such, quantitative PXRD analysis reveals that these compounds exhibit the expected 3×4 W-R structures with evidence of systematic Mo for W substitution.

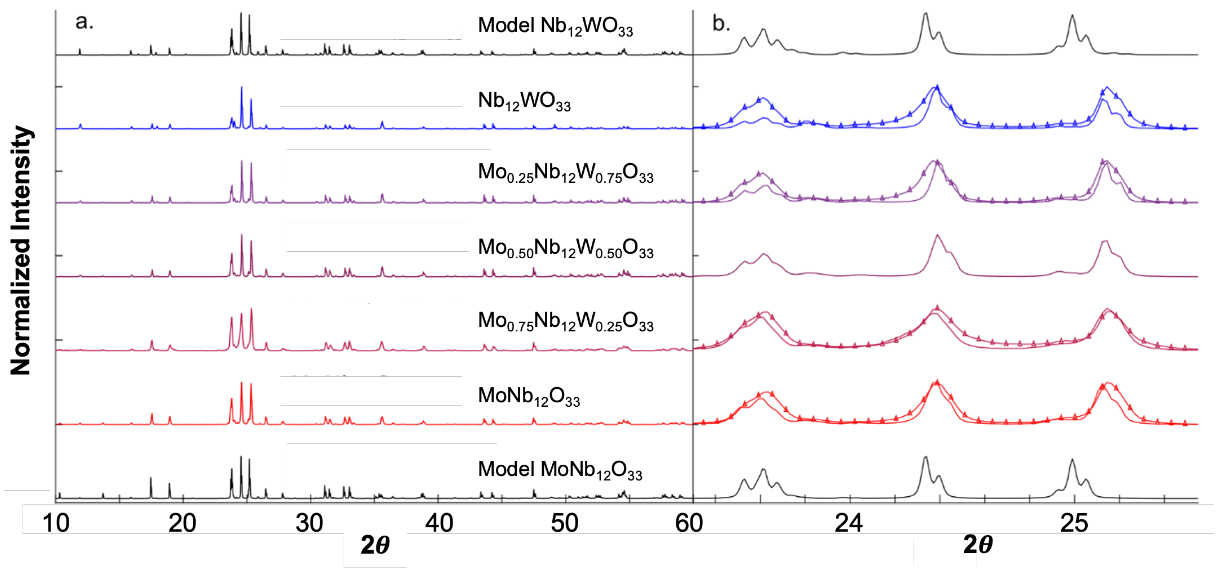

Figure 2. (a) PXRD patterns of $Mo_xNb_{12}W_{1-x}O_{33}$ compounds synthesized for 12 h. The model $Nb_{12}WO_{33}$ and $MoNb_{12}O_{33}$ patterns are also shown at the top and bottom (ICSD collection code 237990 (ref 2) with space group C2). (b) Comparison of PXRD patterns in a limited 2θ region for $Mo_xNb_{12}W_{1-x}O_{33}$ compounds synthesized for 12 h (solid line) and 1 min (solid line connected by triangles). We refer to the samples synthesized for 1 min as defect-rich (D-$Mo_xNb_{12}W_{1-x}O_{33}$) due to the enhanced peak broadening (see main text for details). We normalized the peak intensities in (a-b) with respect to the maximum peak.

The samples heated rapidly and for less total time exhibit diffraction peaks that can also be attributed to the *C*2/*m* space group (Figure S2), indicating that the short reaction condition also yields products with the desired crystallographic shear structure and composition. While no additional peaks are observed, close examination of the PXRD data revealed peak broadening compared to the nearly phase pure samples (Figure 2b). Characterizing these materials via PXRD and Rietveld refinement analysis is challenging due to the possibility of transition metals occupying different sites,[21] and the similarity of atomic scattering factor between Nb and Mo.[71,72] literature evidence strongly suggests that the peak broadening effect is likely due to the presence of other W-R phases or structural defects; Li, et al. showed similar PXRD peak broadening effects in H-Nb_2O_5 samples that could be attributed to structural defects such as intergrowths that could only be confirmed by high resolution electron microscopy.[73] Other possible explanations for the peak broadening include an increased density of crystallographic defects—such as shear-plane disorder and associated strain—characteristic of Wadsley–Roth phases.[46–51] Particle size effects cannot entirely explain the peak broadening effect because SEM imaging (Figure S3-Figure S4) and subsequent particle size analysis (Table S1-Table S2) revealed similar particle morphologies and dimensions, especially for the $MoNb_{12}O_{33}$ samples. Regardless of the exact origin of the peak broadening, we conclude that quickly ramping the temperature to a setpoint and holding the reaction mixture for a short time promotes defect formation. For these reasons, we refer to the samples synthesized rapidly and for a short react time as defect-rich (D-$Mo_xNb_{12}W_{1-x}O_{33}$). We discuss how impurity phases or structural defects could possibly influence the electrochemical properties in the Discussion section.

Next, we utilized Raman spectroscopy to identify the crystallographic sites that Mo or W atoms occupy in the structure. Figure 3a-b compares experimental Raman spectra of the $Mo_xNb_{12}W_{1-x}O_{33}$

and D-$Mo_xNb_{12}W_{1-x}O_{33}$ samples acquired using a 785 nm laser. New peaks appear while others disappear as x increases, suggesting a change in local symmetry from substitution of W by Mo. For example, a shoulder peak at 937 cm^{-1} systematically increases with x as another peak at 979 cm^{-1} monotonically decreases and ultimately disappears when $x = 1$. The peak intensity ratios change between the samples but the peak positions do not (Figure 3c-f), suggesting that the local bonding environments are similar for the samples prepared via two different synthetic conditions. We focus our discussion on the nearly phase pure samples because we observed similar trends for the samples with higher defect densities, D-$Mo_xNb_{12}W_{1-x}O_{33}$ (e.g., the fast heated samples).

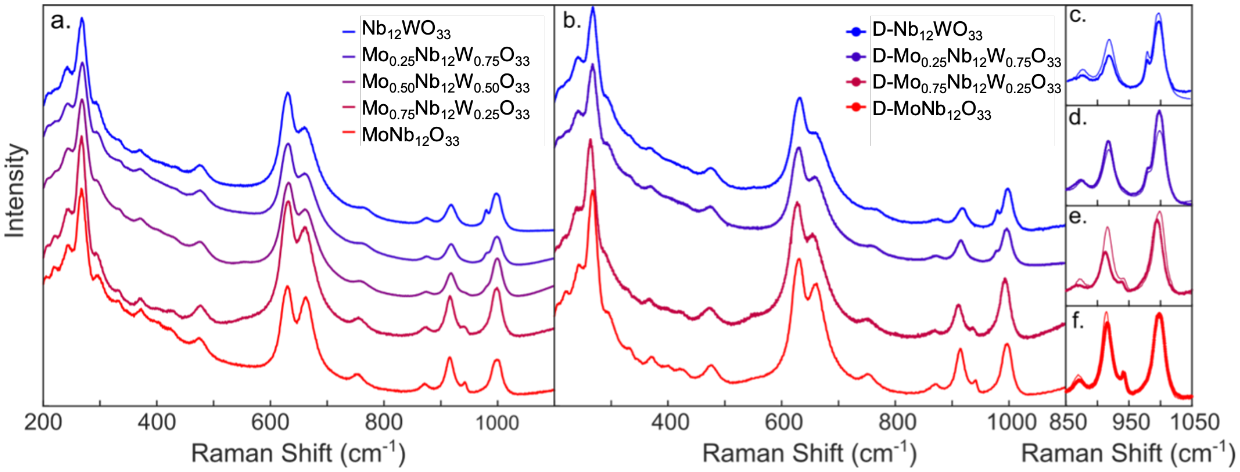

Figure 3. Raman spectra of (a) $Mo_xNb_{12}W_{1-x}O_{33}$ and (b) D-$Mo_xNb_{12}W_{1-x}O_{33}$ samples measured using a 785 nm laser. (c-f) Zoomed-in view of the Raman data to compare $Mo_xNb_{12}W_{1-x}O_{33}$ to D-$Mo_xNb_{12}W_{1-x}O_{33}$ (denoted by the dotted line).

Density functional theory (DFT) based calculations predict that Mo^{6+} and W^{6+} preferentially occupy the tetrahedral sites due to their higher oxidation state than Nb^{5+}, in agreement with Pauling's rules (high charge, low coordination number).[21] To test this hypothesis, we compared

Raman spectroscopy experiments and compared those results to first principles calculations spectra computed with CRYSTAL23 at a hybrid DFT level with 25% exact exchange and POB-TZVP-rev2 basis sets where Mo and W atoms occupy different sites in the unit cell structure. Figure 4 compares experimental Raman spectra of $MoNb_{12}O_{33}$ and $WNb_{12}O_{33}$ acquired at 532 nm and 785 nm with theoretical spectra computed at 532 nm for three site occupancy models. In these models, Mo or W occupies either edge-sharing octahedra along the shear plane, corner-sharing octahedra in the block center, or tetrahedral sites at the block corner, as illustrated in Figure 1a. The peak broadening and shifts observed under 532 nm excitation relative to 785 nm can be attributed to a combination of increased resonance enhancement near charge transfer transitions and greater local laser heating, both of which are amplified at higher photon energies in these mixed metal oxides. Table S3 provides a summary of the calculated Raman modes. For $Nb_{12}WO_{33}$ (Figure 4b), the calculated and experimental spectra exhibit similar energy spacing between the highest-frequency bands when W occupies the tetrahedral site, in agreement with computational predictions and neutron diffraction studies.[21,71] The model with Mo substituting purely on the tetrahedral site captures the experimental spectra across the full range, including the low frequency modes from 200–500 cm^{-1}, the weak band at 760 cm^{-1}, and the high-frequency bands spanning 900–1020 cm^{-1}. The models substituting on either the edge-sharing or corner-sharing octahedral sites introduce narrow bands near 550–600 cm^{-1} that are not observed experimentally. The <400 cm^{-1} region is less sensitive to site occupancy and is instead dominated by tilts and lattice translations of the block framework. The experimental spectra (black traces) show two prominent peaks over the range of 600-700 cm^{-1} that are not fully captured by any site model. However, mode animations reveal that the shoulder at 630 cm^{-1} (Figure S5) and 650 cm^{-1} (Figure S6) likely arises from collective bends of the shear-plane octahedra. Quantitative overlays of calculated and experimental spectra do not require empirical frequency scaling; a uniform offset ≤10 cm^{-1} improves the match for the very highest-frequency band in a few cases and is attributed to residual anharmonicity of the tetrahedral stretch. For $MoNb_{12}O_{33}$ (Figure 4a), the tetrahedral site and edge-sharing models produce similar spectra (green and orange traces, respectively), making it difficult to unambiguously assign the most likely site occupancy. We observe a blue shift of the W tetrahedral stretch relative to Mo. Given the higher mass of W, this shift implies a stiffer W–O bond, as inferred from the DFT frequency assignments. The band at 937 cm^{-1} is assigned to the Mo–O symmetric stretch on the tetrahedral block-corner site, and the band at 979 cm^{-1} is the corresponding W–O(tet) symmetric stretch. In the calculations, these modes are the highest-frequency motions involving the substituent and appear only when Mo or W occupies the tetrahedral site; placing the cation on edge- or interior-octahedral positions suppresses these lines and redistributes intensity into the mid-frequency framework manifold. Experimentally, their presence and relative area provide a direct fingerprint of tetrahedral occupancy by Mo and W. The absolute positions are separated by ~40 cm^{-1} because the stiffer W–O bond shifts the tetrahedral stretch to higher wavenumber, whereas the neighboring Nb–O–Nb framework band sits still higher (~995–1005 cm^{-1}) and remains present irrespective of dopant site. Small sample-to-sample shifts (a few cm^{-1}) are expected with local environment and broadening, but the identity and interpretation of the 937 and 979 cm^{-1} peaks as Mo–O(tet) and W–O(tet) remain robust.

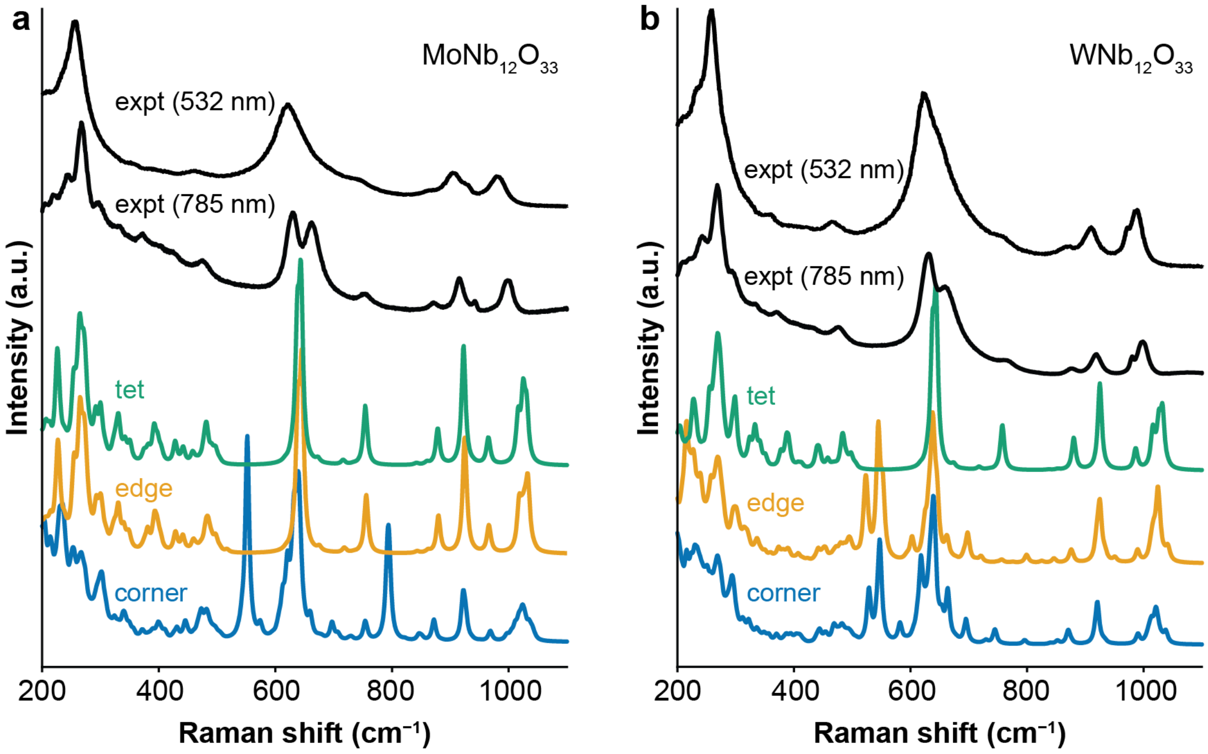

Figure 4. (a) Raman spectra of MoNb$_{12}$O$_{33}$ (C2/m); experimental data (black traces acquired with 532 and 785 nm laser sources) and calculated spectra for 532 nm laser excitation using CRYSTAL23 models with Mo on the tetrahedral site (green trace), edge-shared octahedral sites on the shear plane (orange trace), and corner-sharing octahedra in the block center (blue trace) at PBEsol-hybrid-25/POB-TZVP-rev2 (300 K, 532 nm; Lorentzian FWHM 10–12 cm^{-1}). **(b)** same as for (a), but for WNb$_{12}$O$_{33}$ (C2/m).

In summary, the clear separation and expected relative intensity of the tetrahedral-site high-frequency band relative to the Nb–O–Nb manifold, combined with the A_g/B_g selection rules of the *C*2/*m* phase, offer a strong spectroscopic fingerprint for W occupying the tetrahedral site. However, the corresponding site preference of Mo (whether tetrahedral or the edge-sharing octahedral sites) cannot be resolved from comparison of calculated and experimental Raman spectra alone.

Electrochemical Behavior During Li-ion Insertion. Having characterized the structure and transition metal site occupancy of the $Mo_xNb_{12}W_{1-x}O_{33}$ compounds, we investigated their electrochemical behavior and performance as Li-ion insertion hosts. We constructed coin cells by mixing metal oxide host material, conductive carbon, and PVDF polymer binder in an 8:1:1 ratio. This ratio was utilized to help minimize the ohmic loss (i.e., *iR* loss) due to the intrinsically poorly conductive oxide particles and aid in the mechanical stability and electrical contact upon cycling; the ratio was not optimized for battery performance.[80,81] Additionally, we cycled all cells at a slow C/3 rate to minimize *iR* loss effects in the insulating metal oxide electrodes.

Figure 5a-e shows the charge/discharge behavior for nearly phase pure $Mo_xNb_{12}W_{1-x}O_{33}$ compounds. The compounds exhibit qualitatively similar voltage profiles upon lithiation/de-lithiation (i.e., discharge/charge cycles). Upon lithiation, the potential quickly decreases from 3 V to approximately 2 V vs Li/Li^+ until a plateau region appears at approximately $y = 1$, where y is the number of Li-ions inserted per formula unit. The plateau region persists to approximately $y = 5$. Then, the potential monotonically decreases until the 1 V voltage cutoff limit is defined in our experiment. We observed similar charge-discharge profiles for the D-$Mo_xNb_{12}W_{1-x}O_{33}$ compounds (Figure S7-Figure S8).

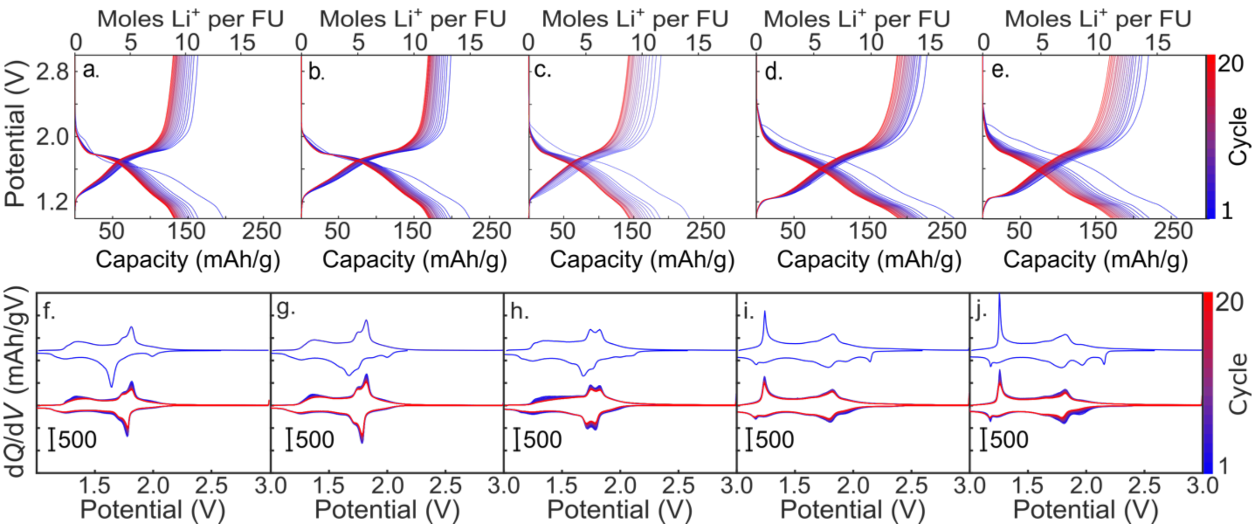

Figure 5. (a-e) Charge-discharge behavior for nearly phase pure $Mo_xNb_{12}W_{1-x}O_{33}$ compounds (a) $Nb_{12}WO_{33}$, (b) $Mo_{0.25}Nb_{12}W_{0.75}O_{33}$, (c) $Mo_{0.50}Nb_{12}W_{0.50}O_{33}$, (d) $Mo_{0.75}Nb_{12}W_{0.25}O_{33}$, and (e) $MoNb_{12}O_{33}$ measured at a C/3 rate for 20 cycles. (f-j) Differential capacity plots obtained from (f) $Nb_{12}WO_{33}$, (g) $Mo_{0.25}Nb_{12}W_{0.75}O_{33}$, (h) $Mo_{0.50}Nb_{12}W_{0.50}O_{33}$, (i) $Mo_{0.75}Nb_{12}W_{0.25}O_{33}$, and (j) $MoNb_{12}O_{33}$ charge-discharge data. The upper blue trace shows the first charge-discharge cycle, and the lower plots represent cycles 2-20.

Several x-dependent trends appear in the charge-discharge data despite their qualitatively similar appearance. First, the plateau region exhibits a slight negative slope, and the slope value increases with x, as evidenced by broader peaks in dQ/dV plots (Figure 5f-j). This enhanced sloping profile feature observed for the Mo-rich compounds is problematic for Li-ion battery applications because a continuously decreasing voltage results in continuous power loss during discharge. Second, Figure 6 shows that all samples exhibit a significant capacity loss between cycles 1 and 2 (also see Figure S9), followed by a continuous capacity fade with additional cycling. The capacity loss rate generally increases with x (Figure S10), possibly due to irreversible structural distortions related to distorted Mo octahedra along the shear plane (see Discussion section for further details). However, the average coulombic efficiency and relative capacity loss plateaus after approximately 4 cycles, and is *x*-independent, for both $Mo_xNb_{12}W_{1-x}O_{33}$ and D-$Mo_xNb_{12}W_{1-x}O_{33}$ (Figure S10-Figure S11). The Discussion section addresses the possible origin of the continuous capacity loss and steady coulombic efficiency in our electrodes. Finally, the most significant observation from Figure 6 is that the discharge capacity systematically increases with *x* (Figure 6, filled circles). In fact, the discharge capacity for $Mo_{0.75}Nb_{12}W_{0.25}O_{33}$ and $MoNb_{12}O_{33}$ exceed the theoretical capacity values for single-electron redox behavior. This trend suggests that substituting Mo for W activates a multi-electron redox behavior whereby transition metal cations undergo multiple reduction events (either Nb^{5+} to Nb^{3+} or Mo^{6+} to Mo^{4+}). Furthermore, we observed that defect-rich samples display similar constant current plots (Figure S7) and generally exhibit greater discharge capacity than the nearly phase pure compounds (see open square symbols in Figure 6), possibly due to Wadsley defects (see Discussion section).

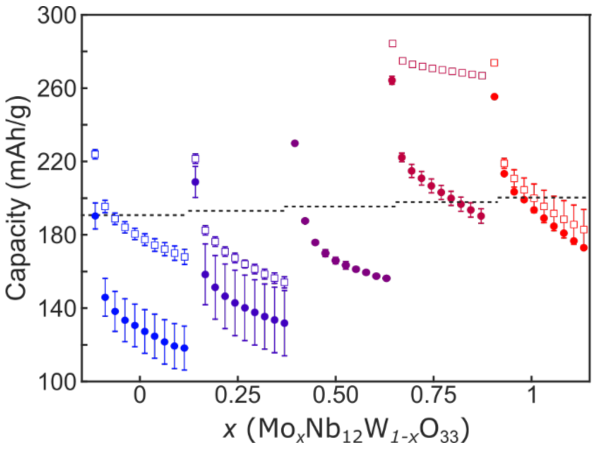

Figure 6. Discharge capacity versus cycle number for nearly phase pure $Mo_xNb_{12}W_{1-x}O_{33}$ (displaying odd cycles only for clarity). The data points represent average values and the error bars

represent the standard error of the mean (see Experimental Methods). The colors correspond to the different compounds in Figure 3. The filled and hollow markers represent $Mo_xNb_{12}W_{1-x}O_{33}$ and D-$Mo_xNb_{12}W_{1-x}O_{33}$ samples, respectively. The horizontal dashed line indicates the theoretical capacity for each composition, assuming single electron redox per Nb, W, or Mo transition metal in the unit cell.

To better understand how Mo-substitution affects the ion insertion electrochemistry and electrochemically accessible DOS, we examined the differential capacity (dQ/dV) plots shown in Figure 5f-j. We discuss the positive potential region (potentials greater than 2 V) of the dQ/dV plots first. Upon inserting a single Li-ion per formula unit in the pristine $x = 0$ and $x = 0.25$ samples during the first cycle (top traces in Figure 5f-g), a single peak appears near 2 V (specifically 1.991 and 1.999 V for $x = 0$ and $x = 0.25$ samples, respectively). These negative dQ/dV peaks do not exhibit a corresponding positive dQ/dV feature upon de-lithiation and do not appear in additional cycles (bottom traces in Figure 5f-j). Both observations suggest the first Li-ion insertion event is irreversible. The peak broadens in the $x = 0.5$ compound and eventually splits into two discernable peaks for the $x = 0.75$ and $x = 1.0$ compounds. Again, we observed no corresponding positive dQ/dV feature upon de-lithiation, suggesting the initial lithiation events are irreversible. In summary, Mo substitution introduces new electrochemically active states at more positive potentials than the W-based compounds.

Next, we analyze the prominent dQ/dV features between 1.5 and 2.0 V. Upon lithiation, the $x = 0$ compound exhibits a sharp negative dQ/dV peak at 1.641 V that accounts for approximately 6 Li-ions per formula unit. The corresponding positive dQ/dV feature appears at a significantly more positive potential (1.8 V). After the significant capacity loss event between cycles 1-2, which we believe is associated with the first Li-ion insertion event, the negative dQ/dV peak shifts to more positive potentials and occurs at nearly the same potential as the positive 1.7 V dQ/dV feature during cycle 1. The peak shift for the negative dQ/dV peak could be explained by an electrical conductivity improvement upon irreversibly introducing 1 Li-ion per formula unit in the initially insulting oxide phase.[21] In this scenario, the dramatic conductivity increase upon lithiation could lower the overpotential associated with filling the electrochemically active DOS. Interestingly, this peak shift effect is most pronounced in the $x = 0$ compound. Substituting Mo for W results in relatively reversible and symmetric dQ/dV features between 1.5 and 2.0 V, which suggests that the Mo-derived electrochemically active DOS is distinct from W-derived states.

Finally, the region between 1.5 and 1.0 V accounts for approximately 6-10 Li-ions per formula unit, depending on x. For $x < 0.5$, a broad peak appears at 1.2 V in the dQ/dV plots (Figure 5f-h). Unlike other peaks at more positive potentials, the negative dQ/dV peak exhibits a corresponding positive peak and neither feature shifts with additional cycle numbers. As Mo content increases, the negative dQ/dV peak sharpens. Additionally, we observe similar trends in the dQ/dV plots for D-$Mo_xNb_{12}W_{1-x}O_{33}$ (Figure S8). These observations suggest a transition from delocalized to localized electrochemically active DOS as Mo substitutes for W (i.e., as x increases). In summary, the dQ/dV plots show that Mo substitution introduces new electrochemically active DOS. The Discussion section considers how the Mo-derived DOS contributes to enhanced capacity.

Electronic Structure Calculations. DFT calculations reveal that both Mo and W based compounds are capable of yielding site disorder, but only Mo substitution for corner-linked Nb sites impacts the frontier electronic states as to yield a change in redox capacity. For each composition $Nb_{12}MO_{33}$ (M = Mo or W), we calculated every symmetrically distinct arrangement of M from 1-3 formula units using the PBEsol GGA functional. Analysis of the energies of these relaxed structures (Figure 7) shows that W and Mo are most stable in the tetrahedral sites. The tetrahedral site is the most stable position by ~4 meV per atom for the W system and ~8 meV per atom for the Mo system, suggesting a lower thermodynamic advantage for disorder in the W system. For convenience, we will refer to any structure with all the tetrahedral sites occupied by *M* as the “ordered” structure. All the low energy “disordered” structures contain a tetrahedrally coordinated dopant in addition to a defective site, where W or Mo occupies a non-ideal corner-sharing or edge-sharing site. Notably, we observe a slight site preference for the tetrahedral and edge-sharing sites for the Mo dopant whereas tetrahedral and corner-sharing preference is observed for W, in general agreement with the Raman results in Figure 4. However, the low energy differences between the sites means that, from a thermodynamic basis, both Mo and W based compounds likely have cation site disorder, consistent with early neutron diffraction studies.[9]

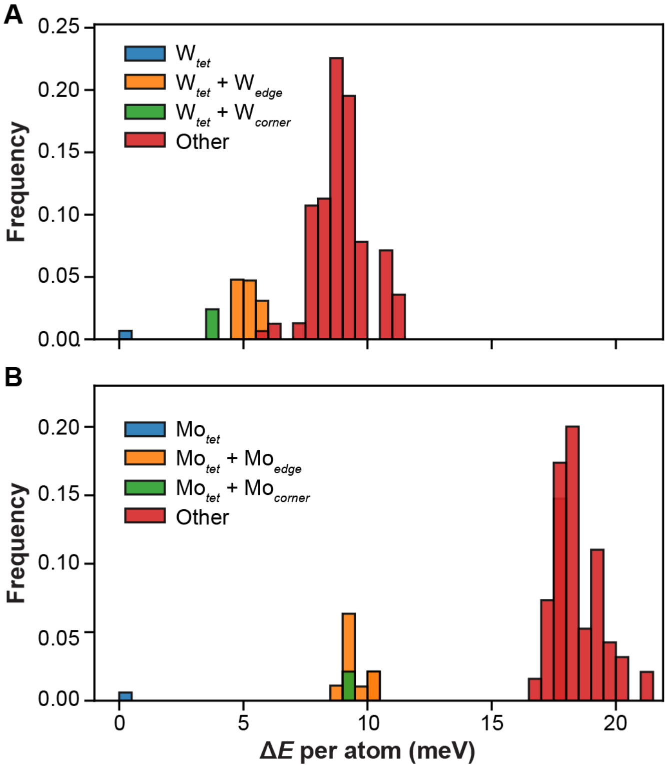

Figure 7. Dopant site energetics for (A) $Nb_{12}WO_{33}$ and (B) $Nb_{12}MoO_{33}$ calculated for every symmetry distinct dopant structure containing two formula units of $Nb_{12}MO_{33}$, where M = Mo or W.

To investigate the effect of electrochemical reduction and Li-ion insertion on the electronic structure, we considered three structures for each composition—one "pristine" structure in which the M atom resides exclusively on the tetrahedral site and two "defective" structures containing a defect pair $[Nb_M + M_{Nb}]$, where the M_{Nb} defect resides on either a corner-sharing or edge-sharing site. These structures were embedded in a supercell generated using the `doped` package to minimize the interactions between defect periodic images following the standard supercell defect methodology.[82,83] Figure 8 shows the conduction band DOS for these structures (i.e., the states most likely to accommodate additional electrons on charging). Mo and W do not significantly contribute to low lying conduction band states when those atoms occupy the tetrahedral site (the ordered structure in Figure 8A-B). The contribution from *M* at the corner-sharing position (Figure 8C-D) and the edge-sharing position (Figure 8E-F) in general is greater, with a larger contribution from Mo than W in general. From these results, it may be expected that the *M* in "defective" positions are more easily reduced than those in ideal tetrahedral positions.

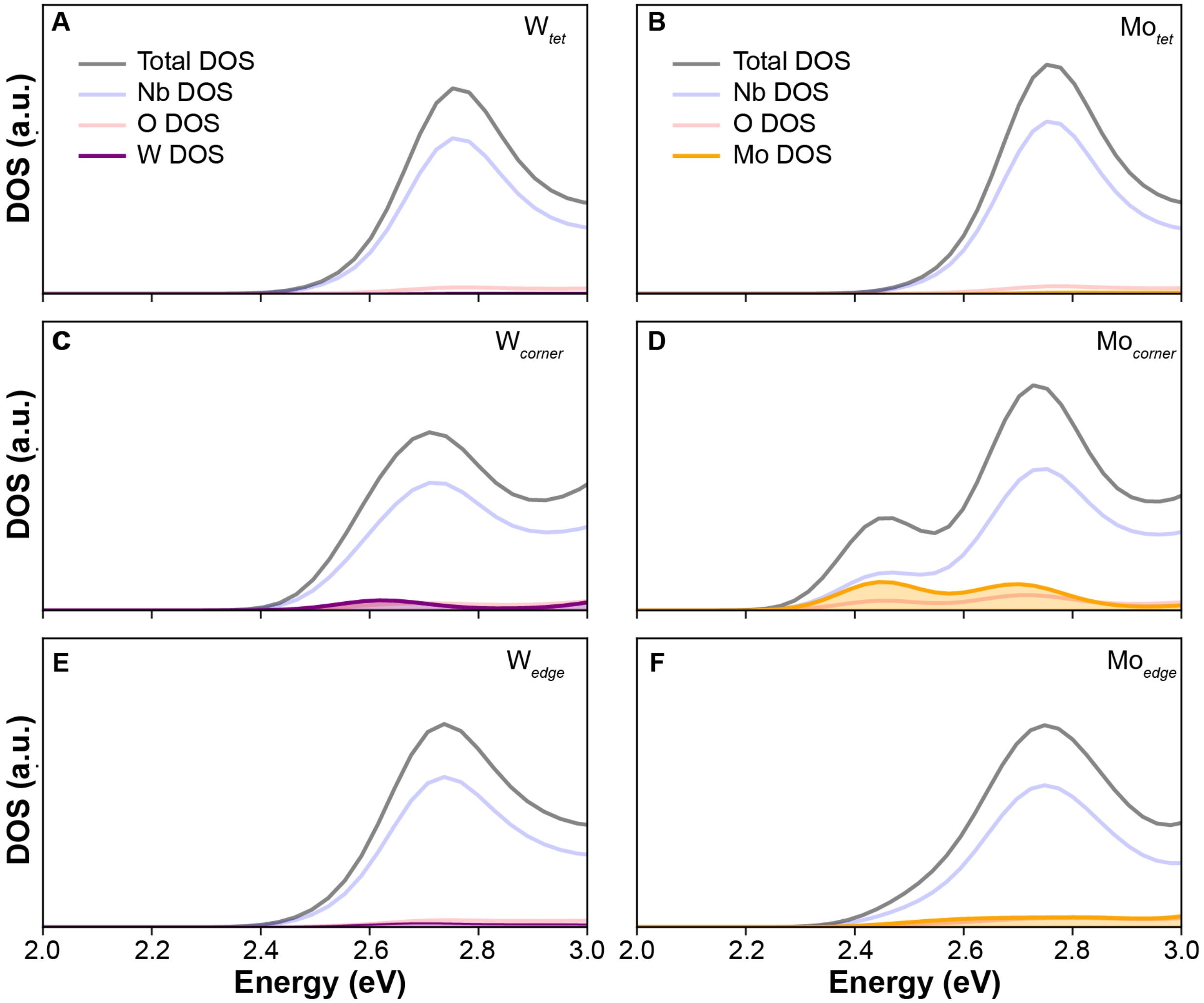

Figure 8. Conduction band minimum density of states for $Nb_{12}MO_{33}$ (*M* = Mo or W). (A-B) DOS calculated for the "pristine" structure where all *M* atoms occupy tetrahedral sites. (C-D) and (E-F)

represent the DOC calculated for two defective structures, where the Mo or W substituted for Nb at a corner-sharing site (C-D) or a shear plane site (E-F). The calculations were performed with the r2SCAN functional.

To establish the first order effect of introducing additional electrons into these different structures, the structures were relaxed after the addition of one and two electrons to simulate the effect of charging the material without introducing the combinatorial problem of enumerating lithium positions. The electronic structure of each compound was then examined by plotting its conduction band DOS as a function of one (Figure 9-left column) and two (Figure 9-right column) electrons inserted and different *M* site occupancies. Upon adding a single electron to structures where *M* occupies corner-sharing sites (Figure 9A,C) or shear plane sites (Figure 9E,G), *M*-localized states are introduced for both *M* species, corresponding to a formal reduction of M^{6+} to M^{5+}. The colored *M* DOS contributes to the total DOS, indicating formal reduction of M^{6+} to M^{5+} when *M* occupies those sites. On the other hand, when *M* occupies the tetrahedral site (Figure 9I,K), *M* sites are redox-inactive. Interestingly, critical differences emerge when the dopant resides at the edge-sharing octahedral site along the shear-plane. Here, Mo can accommodate two electrons (Figure 9F), corresponding to a two-electron reduction process Mo^{6+} -> Mo^{5+} -> Mo^{4+}. The localized states within the host band gap act as electron traps and potentially explain the increased multi-electron capacity of the Mo samples.

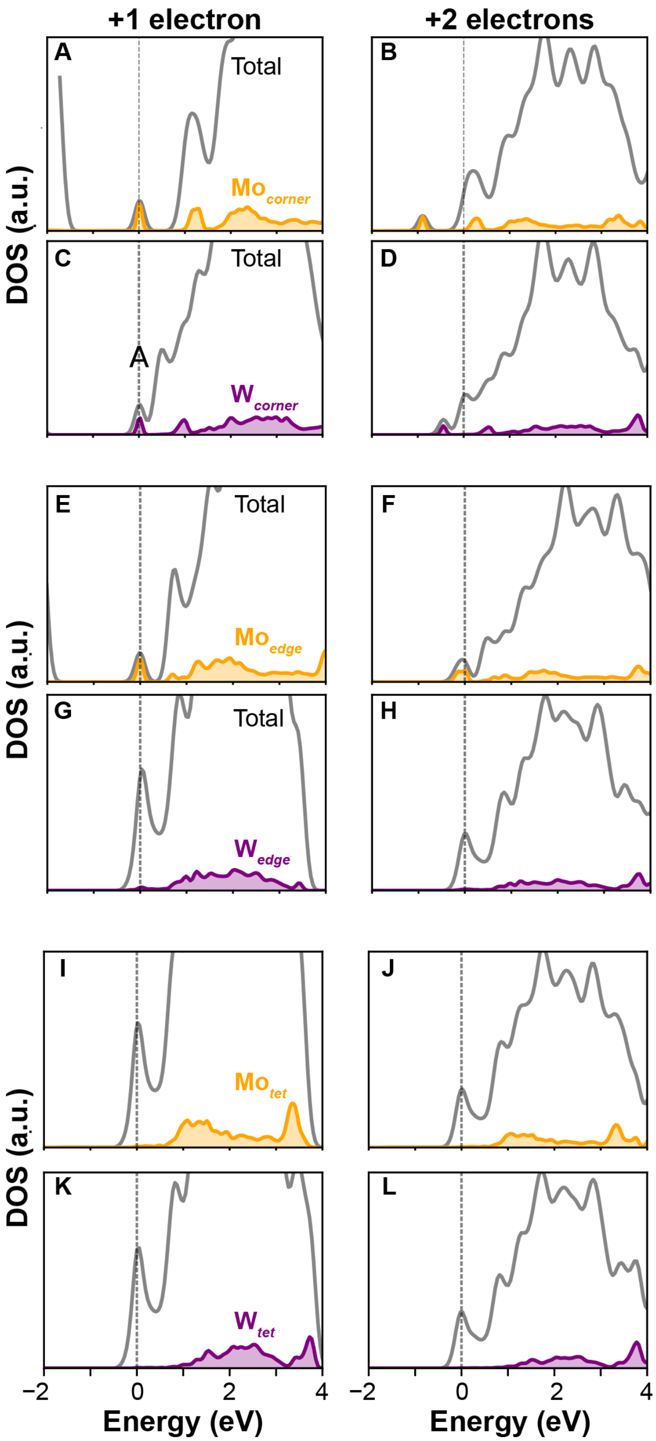

Figure 9. Evolution of $Nb_{12}MO_{33}$ (M = Mo or W) DOS as a function of charge added. The left-hand column shows the DOS after the addition of one electron, while the right-hand column shows the DOS after the addition of two electrons. (A-D) show the DOS when M occupies the corner

sharing site. (E-G) show the DOS when *M* occupies a shear plane site. (I-L) show the DOS when *M* occupies the tetrahedral sites. The vertical line indicates the Fermi energy. The calculations were performed with the r2SCAN functional.

Figure 10 shows the partial charge density associated with the introduction of the two electrons in the *M* shear plane structures for both Mo and W. For Mo, all excess charge density is trapped on the Mo ion (Figure 10A) whereas for W, the charge density is delocalized across the simulation cell (Figure 10B). The key point is that Mo edge-shared octahedra at the shear plane can facilitate a two-electron redox process that is inaccessible to W dopants in all sites or Mo dopants residing in the tetrahedral or corner-sharing site.

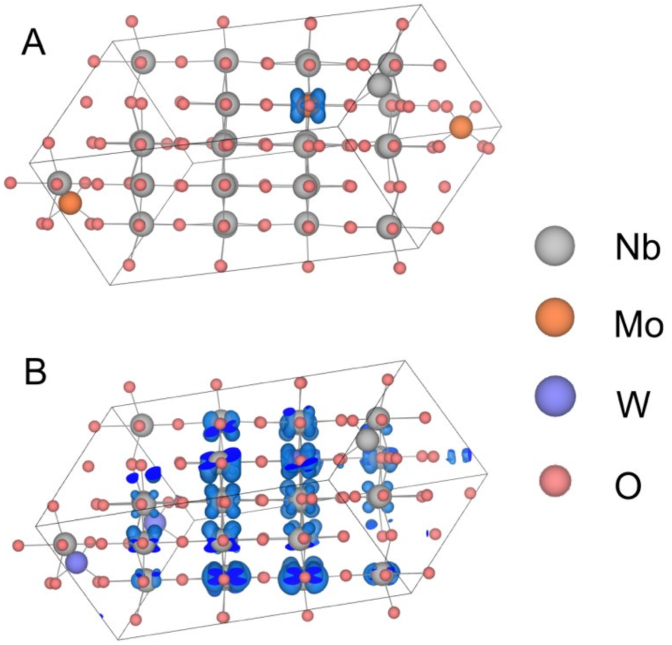

Figure 10. Partial charge density plots from 0.3 eV below the highest occupied state in (A) $Nb_{12}MoO_{33}$ and (B) $Nb_{12}WO_{33}$ when M is at the shear-plane site and when two excess electrons are present in the system (c.f. Figure 9F,H).

Discussion

Here we discuss possible explanations for our 3 key results: (1) defective W-rich W-R samples exhibit greater capacities than nearly phase pure compounds; (2) Mo substitution for W increases capacity and enables multi-electron redox behavior; and (3) Mo substitution enhances capacity loss.

First, we discuss the possible defect phases in the D-$Mo_xNb_{12}W_{1-x}O_{33}$ samples and how those phases could contribute to capacity enhancement. Recall the PXRD patterns for the slowly heated $Mo_xNb_{12}W_{1-x}O_{33}$ samples exhibit narrow, well-defined peaks compared to the rapidly heated D-$Mo_xNb_{12}W_{1-x}O_{33}$ samples (Figure 2). The presence of Wadsley defects, or coherent intergrowths of a W-R family member in another matrix, could possibly explain the peak broadening.[6,7,42,46] For example, $Nb_{26}W_4O_{77}$ is an ordered intergrowth of $Nb_{12}WO_{33}$ and $Nb_{14}W_3O_{44}$.[42,44,45] $Nb_{15}W_6O_{55}$ and H-Nb_2O_5 represent other potential defect phases that can form under the reaction conditions employed herein.[10,26,39] These defects may only extend half a unit cell and, therefore, may not appear in PXRD data.

Wadsley defects can enhance Li-ion insertion capacity of W-R electrodes. Li et al. revealed local rearrangements of [NbO_6] octahedra in micrometer-sized particles of H-Nb_2O_5 using high resolution transmission electron microcopy and showed that those planar Wadsley defects resulted in higher specific capacity, rate capability, and stability compared to more crystalline H-Nb_2O_5

and T-Nb_2O_5 electrodes.[46] The authors attributed the higher capacity to strong Li adsorption (i.e., lower binding energy) on planar defects. Specifically, DFT calculations showed lower Li-ion adsorption energies for defective H-Nb_2O_5 than crystalline H-Nb_2O_5, providing evidence that planar defects can increase the capacity of W-R materials. The authors also claimed that the planar defects relieve strain and minimize volume change, enhancing stability. Similar stability trends appear in our data (Figure S9); the D-$Mo_xNb_{12}W_{1-x}O_{33}$ sample series exhibits greater capacity, especially at lower x. Hence, one interesting future direction toward developing structure-property relationships in W-R anode materials is to systematically introduce Wadsley defects and study how their structure, composition, and concentration influence capacity, rate capability, and cycling stability.

Another significant result from this work is that Mo substitution for W increases capacity of W-R electrodes beyond 1 electron per transition metal site. One hypothesis for this capacity increase is that Mo atoms create local Li-ion binding environments that lower Li-ion binding energies.[21] A literature survey conducted by Ok et al. discovered that Mo is prone to a higher degree of distortion compared to Nb and W.[84] Hence, severely distorted Mo octahedra along the shear plane could create local environments with lower Li-ion binding energetics, resulting in higher capacity.[46] Indeed, our electronic structure calculations show that Mo site occupancy along the shear plane introduces localized states that can accommodate two electrons (Figure 9-Figure 10). An alternative explanation for enhanced capacity in $MoNb_{12}O_{33}$ is metal-metal bonding between edge shared transition metal octahedra along the shear plane. Saber et al. recently performed electronic structure calculations as a function of lithiation in $TiNb_2O_7$, another W-R crystallographic shear compound, and discovered metal-metal bonding can occur at low levels of lithiation (beyond x = 1).[32] The same phenomenon occurs in PNb_9O_{26} and VNb_9O_{26}; lithiation induces Nb-Nb orbital overlap.[25] $Li_xNaNb_7O_{18}$ also exhibits evidence for reversible Nb−Nb bond formation.[85] A signature of metal-metal bonding is electronic states below the Fermi level.[32] Experimentally, we observed sharp dQ/dV peaks at positive potentials (>2.0 V in Figure 5f-j) upon inserting about 1 Li-ion per formula unit in each W-R compound. Interestingly, a 200-300 mV gap exists between the sharp dQ/dV peaks and the next major dQ/dV feature. This gap could represent the energy gap between the localized states below the Fermi level predicted by Saber et al.[32] However, here, we find that the mid gap states are associated with the reduction of M ions, acting as electron traps, where the M ion identity and its position are both crucial in determining the resulting electronic structure of the charged system.

Finally, we discuss how Mo substitution for W leads to enhanced capacity loss. It is possible that the same octahedral tilting mechanism responsible for enhanced capacity (discussed above) is also likely responsible for cycling instability. Koçer et al. conducted first-principles DFT calculations to understand how the crystallographic shear structure promotes cycle stability.[21] Their computational work revealed that the shear plane plays a key role in an anisotropic lattice expansion/contraction mechanism during lithiation/de-lithiation cycles, which buffers the volume expansion of the material. Our work suggests that the degree of second order Jahn-Teller distortion, or the off-centering of the d^0 transition-metal cations that are octahedrally coordinated by oxygen, influence the structural stability of the compound under repeated ion insertion/de-insertion cycles. In this scenario, the distorted Mo octahedra along the shear plane become less off-centered as the Mo oxidation state decreases from Mo^{6+} to Mo^{5+}.[21,32] We hypothesize that structural stability depends on the ability of Mo octahedra along the shear plane to "rock" back and forth during lithiation/de-lithiation cycles. An interesting future research direction is to test the hypothesis that reversible Mo octahedral tilting is essential for long-term cycling stability.

Conclusion

We synthesized a series of molybdenum substituted Nb-W-O compounds with different levels of disorder to investigate how elemental composition and defects influence the electrochemical performance for high-rate energy storage applications. Defect-rich samples exhibited greater discharge capacity at low x, likely due to the presence of Wadsley defect phases that alter Li-ion binding energetics. The discharge capacity also increases with increased molybdenum concentrations for both $Mo_xNb_{12}W_{1-x}O_{33}$ and D-$Mo_xNb_{12}W_{1-x}O_{33}$ samples and even exceeded the theoretical capacity for single electron redox, suggesting that Mo substitution is a promising method to improve discharge capacities in Nb-W-O shear compounds. Mo edge-shared octahedra at the shear plane can facilitate a two-electron redox process that is inaccessible to W dopants in all sites or Mo dopants residing in the tetrahedral or corner-sharing site. The number density of Mo octahedra along the shear plane are likely responsible for the enhanced capacity in $Mo_xNb_{12}W_{1-x}O_{33}$. However, the enhanced capacity in Mo-rich compounds is also associated with enhanced capacity loss, likely due to the inability of severely distorted Mo octahedra from "rocking" back and forth during lithiation/delithiation cycles. The structure-property relationships reported here should extend to other W-R compositions and guide the development of high-rate anode materials for electrochemical energy storage applications.

ASSOCIATED CONTENT

Supporting Information. The following files are available free of charge.

XRD, SEM images, Raman spectroscopy measurements and assignments, Rietveld refinement data, and additional electrochemical measurements (PDF)

AUTHOR INFORMATION

Corresponding Author

*jsambur@colostate.edu

Present Addresses

†Cami Christensen, Department of Chemistry, University of Wisconsin-Madison, Madison, Wisconsin 53706, United States.

†Claire Y. Gervais, Department of Chemistry, University of Washington, 109 Bagley Hall, Box 351700, Seattle, WA 98195-1700

†Danielle R. Lustig, Department of Chemistry, University of Oxford, 12 Mansfield Road, Oxford, OX1 3TA, United Kingdom

Author Contributions

Luke Salzer: Conceptualization, synthesis and electrochemical methodology, validation, formal analysis, investigation, resources, data curation, writing – original draft, writing – review and editing, visualization. **Cami Christensen and Claire Gervais:** synthesis and electrochemical methodology, Raman data acquisition, validation, formal analysis, investigation, data curation, writing – original draft, writing – review and editing. **Alexander G. Squires and Alexis G. Manche:** computational methodology, validation, formal analysis, investigation, data curation, writing, review and editing. **Danielle R. Lustig:** SEM data acquisition, assisted with Raman data acquisition, writing – review and editing. **Amy Prieto:** Assisted with coin cell preparation. **James**

Neilson: Supervision, formal analysis, writing – review and editing. **David Scanlon:** Supervision, formal analysis, writing – review and editing. **Justin Sambur:** Conceptualization, methodology, data curation, writing – original draft, writing – review and editing, visualization, supervision, project administration, funding acquisition. The manuscript was written through contributions of all authors. All authors have given approval to the final version of the manuscript.

† Authors contributed equally to this work

Funding Sources

This work was supported by the National Science Foundation (DMR-2046948). We acknowledge CSU Analytical Core research facilities for data acquisition (SCR_021758).

REFERENCES

(1) Roth, R. S.; Wadsley, A. D. Multiple Phase Formation in the Binary System Nb_2O_5–WO_3. I. Preparation and Identification of Phases. *Acta Cryst* **1965**, *19* (1), 26–32. https://doi.org/10.1107/S0365110X65002712.

(2) Roth, R. S.; Wadsley, A. D. Multiple Phase Formation in the Binary System Nb_2O_5–WO_3. II. The Structure of the Monoclinic Phases $WNb_{12}O_{33}$ and $W_5Nb_{16}O_{55}$. *Acta Cryst* **1965**, *19* (1), 32–38. https://doi.org/10.1107/S0365110X65002724.

(3) Roth, R. S.; Wadsley, A. D. Multiple Phase Formation in the Binary System Nb_2O_5–WO_3. III. The Structures of the Tetragonal Phases $W_3Nb_{14}O_{44}$ and $W_8Nb_{18}O_{69}$. *Acta Cryst* **1965**, *19* (1), 38–42. https://doi.org/10.1107/S0365110X65002736.

(4) Roth, R. S.; Wadsley, A. D. Multiple Phase Formation in the Binary System Nb_2O_5–WO_3. IV. The Block Principle. *Acta Cryst* **1965**, *19* (1), 42–47. https://doi.org/10.1107/S0365110X65002748.

(5) Andersson, S.; Mumme, W. G.; Wadsley, A. D. Multiple Phase Formation in the Binary System Nb_2O_5–WO_3. V. The Structure of $W_4Nb_{26}O_{77}$, an Ordered Intergrowth of the Adjoining Compounds $WNb_{12}O_{33}$ and $W_3Nb_{14}O_{44}$. *Acta Cryst* **1966**, *21* (5), 802–808. https://doi.org/10.1107/S0365110X66003852.

(6) Allpress, J. G.; Sanders, J. V.; Wadsley, A. D. Multiple Phase Formation in the Binary System Nb_2O_5–WO_3. VI. Electron Microscopic Observation and Evaluation of Non-Periodic Shear Structures. *Acta Crystallogr B Struct Sci* **1969**, *25* (6), 1156–1164. https://doi.org/10.1107/S0567740869003669.

(7) Allpress, J. G.; Wadsley, A. D. Multiple Phase Formation in the Binary System Nb2O5-WO3 VII. Intergrowth of H-Nb2O5 and WNb12O33. *Journal of Solid State Chemistry* **1969**, *1* (1), 28–38. https://doi.org/10.1016/0022-4596(69)90005-X.

(8) Roth, R. S.; Wadsley, A. D. Mixed Oxides of Titanium and Niobium: The Crystal Structure of TiNb24O62 (TiO2.12Nb2O5). *Acta Cryst* **1965**, *18* (4), 724–730. https://doi.org/10.1107/S0365110X65001664.

(9) Cava, R. J. Lithium Insertion in Wadsley-Roth Phases Based on Niobium Oxide. *Journal of The Electrochemical Society* **1983**, *130* (12), 2345. https://doi.org/10.1149/1.2119583.

(10) Griffith, K. J.; Wiaderek, K. M.; Cibin, G.; Marbella, L. E.; Grey, C. P. Niobium Tungsten Oxides for High-Rate Lithium-Ion Energy Storage. *Nature* **2018**, *559* (7715), 556–563. https://doi.org/10.1038/s41586-018-0347-0.

(11) Deng, Q.; Fu, Y.; Zhu, C.; Yu, Y. Niobium-Based Oxides Toward Advanced Electrochemical Energy Storage: Recent Advances and Challenges. *Small* **2019**, *15* (32), 1804884. https://doi.org/10.1002/smll.201804884.

(12) Ding, H.; Song, Z.; Zhang, H.; Zhang, H.; Li, X. Niobium-Based Oxide Anodes toward Fast and Safe Energy Storage: A Review. *Materials Today Nano* **2020**, *11*, 100082. https://doi.org/10.1016/j.mtnano.2020.100082.

(13) Yang, Y.; Zhao, J. Wadsley–Roth Crystallographic Shear Structure Niobium-Based Oxides: Promising Anode Materials for High-Safety Lithium-Ion Batteries. *Advanced Science* **2021**, *8* (12), 2004855. https://doi.org/10.1002/advs.202004855.

(14) Zhu, X.; Mao, M.; Lin, Z.; Yue, J.; Li, M.; Lv, T.; Zhou, A.; Hu, Y.-S.; Li, H.; Huang, X.; Chen, L.; Suo, L. Wadsley-Roth Phase Niobium-Based Oxide Anode Promising High Power and Energy Density Aqueous Li-Ion Batteries. *ACS Materials Lett.* **2022**, *4* (9), 1574–1583. https://doi.org/10.1021/acsmaterialslett.2c00462.

(15) Liu, Y.; Russo, P. A.; Montoro, L. A.; Pinna, N. Recent Developments in Nb-Based Oxides with Crystallographic Shear Structures as Anode Materials for High-Rate Lithium-Ion Energy Storage. *Battery Energy* **2023**, *2* (1), 20220037. https://doi.org/10.1002/bte2.20220037.

(16) Ko, S. L.; Dorrell, J. A.; Alter, E. D.; Ta, A. C.; Morris, A. J.; Griffith, K. J. Extreme Defect Tolerance for Electrochemical Intercalation in Wadsley–Roth Structures Demonstrated by Metastable $NaNb_7O_{18}$. *J. Am. Chem. Soc.* **2025**, *147* (10), 8513–8522. https://doi.org/10.1021/jacs.4c16977.

(17) Griffith, K. J.; Harada, Y.; Egusa, S.; Ribas, R. M.; Monteiro, R. S.; Von Dreele, R. B.; Cheetham, A. K.; Cava, R. J.; Grey, C. P.; Goodenough, J. B. Titanium Niobium Oxide: From Discovery to Application in Fast-Charging Lithium-Ion Batteries. *Chem. Mater.* **2021**, *33* (1), 4–18. https://doi.org/10.1021/acs.chemmater.0c02955.

(18) Saber, M.; Reynolds, C.; Li, J.; Pollock, T. M.; Van Der Ven, A. Chemical and Structural Factors Affecting the Stability of Wadsley–Roth Block Phases. *Inorg. Chem.* **2023**, *62* (42), 17317–17332. https://doi.org/10.1021/acs.inorgchem.3c02595.

(19) Muhit, M. A. A.; Wechsler, S. C.; Bare, Z. J. L.; Sturgill, C.; Keerthisinghe, N.; Grasser, M. A.; Morrison, G.; Sutton, C.; Stefik, M.; Zur Loye, H.-C. Comparison of Lithium Diffusion in Isostructural $Ta_{12}MoO_{33}$ and $Nb_{12}MoO_{33}$: Experimental and Computational Insights from Single Crystals. *Chem. Mater.* **2024**, *36* (21), 10626–10639. https://doi.org/10.1021/acs.chemmater.4c02118.

(20) Bare, Z. J. L.; Sturgill, C.; Kumar, M.; Milisavljevic, I.; Zur Loye, H.-C.; Misture, S.; Stefik, M.; Sutton, C. Computational Screening and Experimental Validation of Promising

Wadsley-Roth Niobates. *Chem. Mater.* **2025**, *37* (22), 9072–9082. https://doi.org/10.1021/acs.chemmater.5c01273.

(21) Kocer, C.; Griffith, K.; Grey, C.; Morris, A. Cation Disorder and Lithium Insertion Mechanism of Wadsley-Roth Crystallographic Shear Phases from First Principles. *Journal of the American Chemical Society* **2019**, *141* (38), 15121–15134. https://doi.org/10.1021/jacs.9b06316.

(22) Lv, Z.; Zhu, H.; Meng, W.; Wei, L.; Yang, Y.; Zhang, Y.; Ye, M.; Li, C. C. Cation Mixing in Wadsley-Roth Phase Anode of Lithium-Ion Battery Improves Cycling Stability and Fast Li+ Storage. *Appl. Phys. Rev.* **2021**, *8* (3), 031404. https://doi.org/10.1063/5.0054030.

(23) Wu, Z.; Liang, G.; Kong Pang, W.; Zou, J.; Zhang, W.; Chen, L.; Ji, X.; Didier, C.; Peterson, V. K.; Segre, C. U.; Johannessen, B.; Guo, Z. Structural Distortion in the Wadsley-Roth Niobium Molybdenum Oxide Phase Triggering Extraordinarily Stable Battery Performance. *Angewandte Chemie* **2024**, *136* (9), e202317941. https://doi.org/10.1002/ange.202317941.

(24) Voskanyan, A. A.; Navrotsky, A. Shear Pleasure: The Structure, Formation, and Thermodynamics of Crystallographic Shear Phases. *Annu. Rev. Mater. Res.* **2021**, *51* (1), 521–540. https://doi.org/10.1146/annurev-matsci-070720-013445.

(25) Preefer, M. B.; Saber, M.; Wei, Q.; Bashian, N. H.; Bocarsly, J. D.; Zhang, W.; Lee, G.; Milam-guerrero, J.; Howard, E. S.; Vincent, R. C.; Melot, B. C.; Ven, A. V. D.; Seshadri, R.; Dunn, B. S. Multielectron Redox and Insulator-to-Metal Transition upon Lithium Insertion in the Fast-Charging, Wadsley-Roth Phase PNb 9 O 25. **2020**. https://doi.org/10.1021/acs.chemmater.0c00560.

(26) Griffith, K. J.; Forse, A. C.; Griffin, J. M.; Grey, C. P. High-Rate Intercalation without Nanostructuring in Metastable Nb2O5 Bronze Phases. *Journal of the American Chemical Society* **2016**, *138* (28), 8888–8899. https://doi.org/10.1021/jacs.6b04345.

(27) Griffith, K. J.; Grey, C. P. Superionic Lithium Intercalation through 2 × 2 Nm 2 Columns in the Crystallographic Shear Phase Nb 18 W 8 O 69. *Chemistry of Materials* **2020**, *32* (9), 3860–3868. https://doi.org/10.1021/acs.chemmater.9b05403.

(28) Griffith, K. J.; Seymour, I. D.; Hope, M. A.; Butala, M. M.; Lamontagne, L. K.; Preefer, M. B.; Koçer, C. P.; Henkelman, G.; Morris, A. J.; Cliffe, M. J.; Dutton, S. E.; Grey, C. P. Ionic and Electronic Conduction in TiNb2O7. *Journal of the American Chemical Society* **2019**, *141* (42), 16706–16725. https://doi.org/10.1021/jacs.9b06669.

(29) Griffith, K. J.; Senyshyn, A.; Grey, C. P. Structural Stability from Crystallographic Shear in TiO2-Nb2O5 Phases: Cation Ordering and Lithiation Behavior of TiNb24O62. *Inorganic Chemistry* **2017**, *56* (7), 4002–4010. https://doi.org/10.1021/acs.inorgchem.6b03154.

(30) Cheng, Q.; Chen, J.; Zhao, J.; Li, F. A V-Doped W3Nb14O44 Anode in a Wadsley–Roth Structure for Ultra-Fast Lithium-Ion Half/Full Batteries. *New J. Chem.* **2023**, *47* (42), 19537–19545. https://doi.org/10.1039/D3NJ03462C.

(31) Wyckoff, K. E.; Zohar, A.; Li, T.; Zhou, Y.; Kautzsch, L.; Wang, W.; Kepper, A.; Patterson, A. R.; Mandujano, H. C.; Koirala, K. P.; Kallistova, A.; Xu, W.; Liu, J.; Pilon, L.; Cheetham, A. K.; Seshadri, R. Metallicity, Atomic Disorder, and Li-Ion Storage in Fast-Charging Anodes. *J. Am. Chem. Soc.* **2025**, *147* (37), 33432–33441. https://doi.org/10.1021/jacs.5c06578.

(32) Saber, M.; Behara, S. S.; Van der Ven, A. Redox Mechanisms, Structural Changes, and Electrochemistry of the Wadsley–Roth LixTiNb2O7 Electrode Material. *Chem. Mater.* **2023**, *35* (22), 9657–9668. https://doi.org/10.1021/acs.chemmater.3c02003.

(33) Wyckoff, K. E.; Kaufman, J. L.; Baek, S. W.; Dolle, C.; Zak, J. J.; Bienz, J.; Kautzsch, L.; Vincent, R. C.; Zohar, A.; See, K. A.; Eggeler, Y. M.; Pilon, L.; Van der Ven, A.; Seshadri, R. Metal–Metal Bonding as an Electrode Design Principle in the Low-Strain Cluster Compound LiScMo3O8. *J. Am. Chem. Soc.* **2022**, *144* (13), 5841–5854. https://doi.org/10.1021/jacs.1c12070.

(34) Ra, H.-S.; Ok, K. M.; Halasyamani, P. S. Combining Second-Order Jahn−Teller Distorted Cations to Create Highly Efficient SHG Materials: Synthesis, Characterization, and NLO Properties of $BaTeM_2$ O_9 (M = Mo^{6+} or W^{6+}). *J. Am. Chem. Soc.* **2003**, *125* (26), 7764–7765. https://doi.org/10.1021/ja035314b.

(35) Zhu, X.; Xu, J.; Luo, Y.; Fu, Q.; Liang, G.; Luo, L.; Chen, Y.; Lin, C.; Zhao, X. S. MoNb12O33 as a New Anode Material for High-Capacity, Safe, Rapid and Durable Li+ Storage: Structural Characteristics, Electrochemical Properties and Working Mechanisms. *J. Mater. Chem. A* **2019**, *7* (11), 6522–6532. https://doi.org/10.1039/C9TA00309F.

(36) Yang, Y.; Ma, Z.; Wang, Q.; Lu, Z.; Jia, T.; Liu, G.; Liu, Y.; Yang, Z.; Wang, S.; Liu, X. Facile Synthesis of Urchin-like MoNb12O33 Microspheres with a Superior Performance as an Anode Material for Lithium-Ion Half/Full Batteries. *Journal of Alloys and Compounds* **2023**, *941*, 168982. https://doi.org/10.1016/j.jallcom.2023.168982.

(37) Deng, Z.; Shi, S.; Mou, P.; Du, C.; Wan, G.; Wang, G. A Lamellar MoNb12O33 as the High-Rate Anode Material for Lithium-Ion Batteries. *J. Electron. Mater.* **2022**, *51* (8), 4125–4132. https://doi.org/10.1007/s11664-022-09706-4.

(38) Lakhdar, Y.; Chen, Y.; Geary, H.; Houck, M. E.; Groombridge, A. S.; Slater, P. R.; Kendrick, E. Toward Higher-Power Li-Ion Batteries: Unravelling Kinetics and Thermodynamics of MoNb12O33 vs. NMC622. *Journal of Power Sources* **2023**, *588*, 233710. https://doi.org/10.1016/j.jpowsour.2023.233710.

(39) Salzer, L. D.; Diamond, B.; Nieto, K.; Evans, R. C.; Prieto, A. L.; Sambur, J. B. Structure–Property Relationships in High-Rate Anode Materials Based on Niobium Tungsten Oxide Shear Structures. *ACS Appl. Energy Mater.* **2023**, *6* (3), 1685–1691. https://doi.org/10.1021/acsaem.2c03573.

(40) Koçer, C. P.; Griffith, K. J.; Grey, C. P.; Morris, A. J. Cation Disorder and Lithium Insertion Mechanism of Wadsley-Roth Crystallographic Shear Phases from First Principles. *Journal of the American Chemical Society* **2019**, *141* (38). https://doi.org/10.1021/jacs.9b06316.

(41) Koçer, C. P.; Griffith, K. J.; Grey, C. P.; Morris, A. J. Lithium Diffusion in Niobium Tungsten Oxide Shear Structures. *Chemistry of Materials* **2020**. https://doi.org/10.1021/acs.chemmater.0c00483.

(42) Allpress, J. G.; Roth, R. S. The Effect of Annealing on the Concentration of Wadsley Defects in the Nb2O5-WO3 System. *Journal of Solid State Chemistry* **1971**, *3* (2), 209–216. https://doi.org/10.1016/0022-4596(71)90030-2.

(43) Cardon, P.; Adams, S.; Crites, E.; Kushwaha, S.; Smith, S.; McQueen, T.; Ji, H. Intrinsic Structures and Electrochemical Properties of Floating Zone Grown Nb_{12} WO_{33} and Nb_{14} W_3 O_{44} Single Crystals. *Crystal Growth & Design* **2025**, *25* (4), 1265–1275. https://doi.org/10.1021/acs.cgd.4c01704.

(44) Andersson, S.; Mumme, W. G.; Wadsley, A. D. Multiple Phase Formation in the Binary System Nb2O5–WO3. The Structure of W4Nb26O77, an Ordered Intergrowth of the Adjoining Compounds WNb12O33 and W3Nb14O44 - Andersson - 1966 - Acta Crystallographica - Wiley Online Library. *Acta Crystallographica* **1966**, *21*.

(45) Li, D. X.; Kuo, K. H. High-Resolution Electron Microscopy of Defects in W4Nb26O77. *Journal of Solid State Chemistry* **1985**, *56* (2), 236–240. https://doi.org/10.1016/0022-4596(85)90061-1.

(46) Li, T.; Nam, G.; Liu, K.; Wang, J.-H.; Zhao, B.; Ding, Y.; Soule, L.; Avdeev, M.; Luo, Z.; Zhang, W.; Yuan, T.; Jing, P.; Gyu Kim, M.; Song, Y.; Liu, M. A Niobium Oxide with a Shear Structure and Planar Defects for High-Power Lithium Ion Batteries. *Energy & Environmental Science* **2022**, *15* (1), 254–264. https://doi.org/10.1039/D1EE02664J.

(47) Saritha, D.; Pralong, V.; Varadaraju, U. V.; Raveau, B. Electrochemical Li Insertion Studies on WNb12O33—A Shear ReO3 Type Structure. *Journal of Solid State Chemistry* **2010**, *183* (5), 988–993. https://doi.org/10.1016/j.jssc.2010.03.003.

(48) Faraji, S.; Ani, F. N. Microwave-Assisted Synthesis of Metal Oxide/Hydroxide Composite Electrodes for High Power Supercapacitors - A Review. *Journal of Power Sources* **2014**, *263*, 338–360. https://doi.org/10.1016/j.jpowsour.2014.03.144.

(49) Zhu, X.; Xu, J.; Luo, Y.; Fu, Q.; Liang, G.; Luo, L.; Chen, Y.; Lin, C.; Zhao, X. S. MoNb12O33 as a New Anode Material for High-Capacity, Safe, Rapid and Durable Li+ Storage: Structural Characteristics, Electrochemical Properties and Working Mechanisms. *Journal of Materials Chemistry A* **2019**, *7* (11), 6522–6532. https://doi.org/10.1039/c9ta00309f.

(50) Roth, R. S.; Wadsley, A. D. Multiple Phase Formation in the Binary System Nb2O5–WO3. II. The Structure of the Monoclinic Phases WNb12O33 and W5Nb16O55. *Acta Cryst* **1965**, *19* (1), 32–38. https://doi.org/10.1107/S0365110X65002724.

(51) Kresse, G.; Hafner, J. Ab Initio Molecular-Dynamics Simulation of the Liquid-Metal--Amorphous-Semiconductor Transition in Germanium. *Phys. Rev. B* **1994**, *49* (20), 14251–14269. https://doi.org/10.1103/PhysRevB.49.14251.

(52) Kresse, G.; Furthmüller, J. Efficiency of Ab-Initio Total Energy Calculations for Metals and Semiconductors Using a Plane-Wave Basis Set. *Computational Materials Science* **1996**, *6* (1), 15–50. https://doi.org/10.1016/0927-0256(96)00008-0.

(53) Perdew, J. P.; Ruzsinszky, A.; Csonka, G. I.; Vydrov, O. A.; Scuseria, G. E.; Constantin, L. A.; Zhou, X.; Burke, K. Restoring the Density-Gradient Expansion for Exchange in Solids and Surfaces. *Phys. Rev. Lett.* **2008**, *100* (13), 136406. https://doi.org/10.1103/PhysRevLett.100.136406.

(54) Furness, J. W.; Kaplan, A. D.; Ning, J.; Perdew, J. P.; Sun, J. Accurate and Numerically Efficient r2SCAN Meta-Generalized Gradient Approximation. *J. Phys. Chem. Lett.* **2020**, *11* (19), 8208–8215. https://doi.org/10.1021/acs.jpclett.0c02405.

(55) Ong, S. P.; Richards, W. D.; Jain, A.; Hautier, G.; Kocher, M.; Cholia, S.; Gunter, D.; Chevrier, V. L.; Persson, K. A.; Ceder, G. Python Materials Genomics (Pymatgen): A Robust, Open-Source Python Library for Materials Analysis. *Computational Materials Science* **2013**, *68*, 314–319. https://doi.org/10.1016/j.commatsci.2012.10.028.

(56) Harris, C. R.; Millman, K. J.; van der Walt, S. J.; Gommers, R.; Virtanen, P.; Cournapeau, D.; Wieser, E.; Taylor, J.; Berg, S.; Smith, N. J.; Kern, R.; Picus, M.; Hoyer, S.; van Kerkwijk, M. H.; Brett, M.; Haldane, A.; del Río, J. F.; Wiebe, M.; Peterson, P.; Gérard-Marchant, P.; Sheppard, K.; Reddy, T.; Weckesser, W.; Abbasi, H.; Gohlke, C.; Oliphant, T. E. Array Programming with NumPy. *Nature* **2020**, *585* (7825), 357–362. https://doi.org/10.1038/s41586-020-2649-2.

(57) Kavanagh, S. R.; Squires, A. G.; Nicolson, A.; Mosquera-Lois, I.; Ganose, A. M.; Zhu, B.; Brlec, K.; Walsh, A.; Scanlon, D. O. Doped: Python Toolkit for Robust and Repeatable

Charged Defect Supercell Calculations. *Journal of Open Source Software* **2024**, *9* (96), 6433. https://doi.org/10.21105/joss.06433.

(58) Hjorth Larsen, A.; Jørgen Mortensen, J.; Blomqvist, J.; Castelli, I. E.; Christensen, R.; Dułak, M.; Friis, J.; Groves, M. N.; Hammer, B.; Hargus, C.; Hermes, E. D.; Jennings, P. C.; Bjerre Jensen, P.; Kermode, J.; Kitchin, J. R.; Leonhard Kolsbjerg, E.; Kubal, J.; Kaasbjerg, K.; Lysgaard, S.; Bergmann Maronsson, J.; Maxson, T.; Olsen, T.; Pastewka, L.; Peterson, A.; Rostgaard, C.; Schiøtz, J.; Schütt, O.; Strange, M.; Thygesen, K. S.; Vegge, T.; Vilhelmsen, L.; Walter, M.; Zeng, Z.; Jacobsen, K. W. The Atomic Simulation Environment—a Python Library for Working with Atoms. *J. Phys.: Condens. Matter* **2017**, *29* (27), 273002. https://doi.org/10.1088/1361-648X/aa680e.

(59) Ångqvist, M.; Muñoz, W. A.; Rahm, J. M.; Fransson, E.; Durniak, C.; Rozyczko, P.; Rod, T. H.; Erhart, P. ICET – A Python Library for Constructing and Sampling Alloy Cluster Expansions. *Advanced Theory and Simulations* **2019**, *2* (7), 1900015. https://doi.org/10.1002/adts.201900015.

(60) Morgan, B. J. Bsym: A Basic Symmetry Module. *Journal of Open Source Software* **2017**, *2* (16), 370. https://doi.org/10.21105/joss.00370.

(61) Erba, A.; Desmarais, J. K.; Casassa, S.; Civalleri, B.; Donà, L.; Bush, I. J.; Searle, B.; Maschio, L.; Edith-Daga, L.; Cossard, A.; Ribaldone, C.; Ascrizzi, E.; Marana, N. L.; Flament, J.-P.; Kirtman, B. CRYSTAL23: A Program for Computational Solid State Physics and Chemistry. *J. Chem. Theory Comput.* **2023**, *19* (20), 6891–6932. https://doi.org/10.1021/acs.jctc.2c00958.

(62) Maschio, L.; Kirtman, B.; Rérat, M.; Orlando, R.; Dovesi, R. Ab Initio Analytical Raman Intensities for Periodic Systems through a Coupled Perturbed Hartree-Fock/Kohn-Sham Method in an Atomic Orbital Basis. I. Theory. *The Journal of Chemical Physics* **2013**, *139* (16), 164101. https://doi.org/10.1063/1.4824442.

(63) Adamo, C.; Barone, V. Toward Reliable Density Functional Methods without Adjustable Parameters: The PBE0 Model. *J. Chem. Phys.* **1999**, *110* (13), 6158–6170. https://doi.org/10.1063/1.478522.

(64) Schimka, L.; Harl, J.; Kresse, G. Improved Hybrid Functional for Solids: The HSEsol Functional. *J. Chem. Phys.* **2011**, *134* (2), 024116. https://doi.org/10.1063/1.3524336.

(65) Peintinger, M. F.; Oliveira, D. V.; Bredow, T. Consistent Gaussian Basis Sets of Triple-Zeta Valence with Polarization Quality for Solid-State Calculations. *Journal of Computational Chemistry* **2013**, *34* (6), 451–459. https://doi.org/10.1002/jcc.23153.

(66) Vilela Oliveira, D.; Laun, J.; Peintinger, M. F.; Bredow, T. BSSE-Correction Scheme for Consistent Gaussian Basis Sets of Double- and Triple-Zeta Valence with Polarization Quality for Solid-State Calculations. *Journal of Computational Chemistry* **2019**, *40* (27), 2364–2376. https://doi.org/10.1002/jcc.26013.

(67) Maschio, L.; Kirtman, B.; Rérat, M.; Orlando, R.; Dovesi, R. Ab Initio Analytical Raman Intensities for Periodic Systems through a Coupled Perturbed Hartree-Fock/Kohn-Sham Method in an Atomic Orbital Basis. II. Validation and Comparison with Experiments. *The Journal of Chemical Physics* **2013**, *139* (16), 164102. https://doi.org/10.1063/1.4824443.

(68) Togo, A. First-Principles Phonon Calculations with Phonopy and Phono3py. *J. Phys. Soc. Jpn.* **2023**, *92* (1), 012001. https://doi.org/10.7566/JPSJ.92.012001.

(69) Lakhnot, A. S.; Gupta, T.; Singh, Y.; Hundekar, P.; Jain, R.; Han, F.; Koratkar, N. Aqueous Lithium-Ion Batteries with Niobium Tungsten Oxide Anodes for Superior Volumetric and

Rate Capability. *Energy Storage Materials* **2020**, *27*, 506–513. https://doi.org/10.1016/j.ensm.2019.12.012.

(70) Krumeich, F. The Complex Crystal Chemistry of Niobium Tungsten Oxides. *Chem. Mater.* **2022**, *34* (3), 911–934. https://doi.org/10.1021/acs.chemmater.1c03723.

(71) Cheetham, A. K.; Allen, N.C. Cation Distribution in the Complex Oxide, W3Nb14044; a Time-of-Flight Neutron Diffraction Study. *J. Chem. Soc. Commun* **1983**, 3.

(72) Maslen, E. N.; Fox, A. G.; O'Keefe, M. A. Atomic Scattering Factor. *International Tables for Crystallography Volume C* **2006**, *C*, 554–595. https://doi.org/10.1107/97809553602060000600.

(73) Hahn, B. P.; Long, J. W.; Mansour, A. N.; Pettigrew, K. A.; Osofsky, M. S.; Rolison, D. R. Electrochemical Li-Ion Storage in Defect Spinel Iron Oxides: The Critical Role of Cation Vacancies. *Energy and Environmental Science* **2011**, *4* (4), 1495–1502. https://doi.org/10.1039/c0ee00819b.

(74) Muniz, F. T. L.; Miranda, M. a. R.; Morilla dos Santos, C.; Sasaki, J. M. The Scherrer Equation and the Dynamical Theory of X-Ray Diffraction. *Acta Cryst A* **2016**, *72* (3), 385–390. https://doi.org/10.1107/S205327331600365X.

(75) Nath, D.; Singh, F.; Das, R. X-Ray Diffraction Analysis by Williamson-Hall, Halder-Wagner and Size-Strain Plot Methods of CdSe Nanoparticles- a Comparative Study. *Materials Chemistry and Physics* **2020**, *239*, 122021. https://doi.org/10.1016/j.matchemphys.2019.122021.

(76) Yogamalar, R.; Srinivasan, R.; Vinu, A.; Ariga, K.; Bose, A. C. X-Ray Peak Broadening Analysis in ZnO Nanoparticles. *Solid State Communications* **2009**, *149* (43), 1919–1923. https://doi.org/10.1016/j.ssc.2009.07.043.

(77) Balogh, L.; Ribárik, G.; Ungár, T. Stacking Faults and Twin Boundaries in Fcc Crystals Determined by X-Ray Diffraction Profile Analysis. *Journal of Applied Physics* **2006**, *100* (2), 023512. https://doi.org/10.1063/1.2216195.

(78) Warren, B. E. X-Ray Studies of Deformed Metals. *Progress in Metal Physics* **1959**, *8*, 147–202. https://doi.org/10.1016/0502-8205(59)90015-2.

(79) Pujar, V. V.; Cawley, J. D. Effect of Stacking Faults on the X-Ray Diffraction Profiles of β-SiC Powders. *Journal of the American Ceramic Society* **1995**, *78* (3), 774–782. https://doi.org/10.1111/j.1151-2916.1995.tb08246.x.

(80) Jiang, J.; Li, Y.; Liu, J.; Huang, X.; Yuan, C.; Lou, X. W. (David). Recent Advances in Metal Oxide-Based Electrode Architecture Design for Electrochemical Energy Storage. *Advanced Materials* **2012**, *24* (38), 5166–5180. https://doi.org/10.1002/adma.201202146.

(81) Itou, Y.; Ogihara, N.; Kawauchi, S. Role of Conductive Carbon in Porous Li-Ion Battery Electrodes Revealed by Electrochemical Impedance Spectroscopy Using a Symmetric Cell. *J. Phys. Chem. C* **2020**, *124* (10), 5559–5564. https://doi.org/10.1021/acs.jpcc.9b11929.

(82) Kim, S.; Hood, S. N.; Park, J.-S.; Whalley, L. D.; Walsh, A. Quick-Start Guide for First-Principles Modelling of Point Defects in Crystalline Materials. *J. Phys. Energy* **2020**, *2* (3), 036001. https://doi.org/10.1088/2515-7655/aba081.

(83) Squires, A. G.; Kavanagh, S.; Walsh, A.; Scanlon, D. Guidelines for Robust and Reproducible Point Defect Simulations in Crystals. Chemistry September 26, 2025. https://doi.org/10.26434/chemrxiv-2025-3lb5k.

(84) Ok, K. M.; Halasyamani, P. S.; Casanova, D.; Llunell, M.; Alemany, P.; Alvarez, S. Distortions in Octahedrally Coordinated D0 Transition Metal Oxides: A Continuous

Symmetry Measures Approach. *Chem. Mater.* **2006**, *18* (14), 3176–3183. https://doi.org/10.1021/cm0604817.

(85) Ko, S. L.; Dorrell, J. A.; Alter, E. D.; Ta, A. C.; Morris, A. J.; Griffith, K. J. Extreme Defect Tolerance for Electrochemical Intercalation in Wadsley–Roth Structures Demonstrated by Metastable $NaNb_7 O_{18}$. *J. Am. Chem. Soc.* **2025**, *147* (10), 8513–8522. https://doi.org/10.1021/jacs.4c16977.

Supplementary information for

Mo Occupancy Along Crystallographic Shear Planes in the Wadsley–Roth Compound $Mo_xNb_{12}W_{1-x}O_{33}$ Enables Multi-Electron Redox Behavior

Luke D. Salzer,[†,a] *Cami Christensen,*[†,a] *Claire Y. Gervais,*[a] *Alexander G. Squires,*[b] *Alexis G. Manche,*[b] *Danielle R. Lustig,*[a] *Amy L. Prieto,*[a] *James R. Neilson,*[a] *David O. Scanlon,*[b] *Justin B. Sambur*[*,a]

[a]Department of Chemistry, Colorado State University, Fort Collins, CO 80523, USA

[b]School of Chemistry, University of Birmingham, Edgbaston, B15 2TT

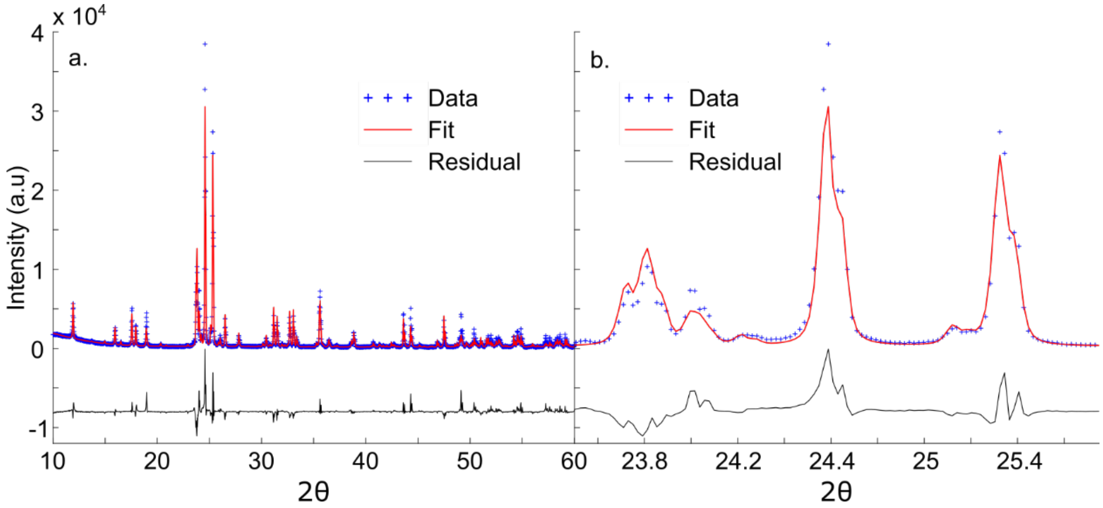

Figure S1. (a) Rietveld refinement of the slowly synthesized $Nb_{12}WO_{33}$ using the C2/m space group (R_{wp} of 20.452). (b) Zoomed-in view of the data in panel (a). The original lattice parameters for the model were 22.370Å, 3.825Å, 17.87Å, and 123.6° for a, b, c, and β respectively. The refined lattice parameters were 22.303Å, 3.826Å, 17.746Å, and 123.346° for a, b, c, and β respectively.

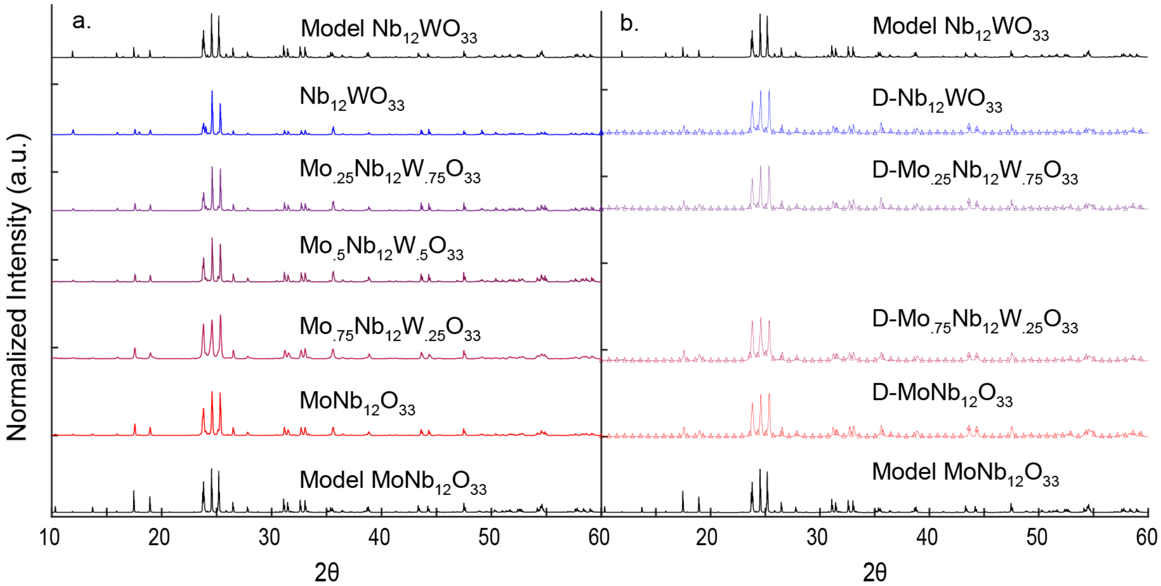

Figure S2. Comparison of simulated and experimental diffraction patterns for (a) $Mo_xNb_{12}W_{1-x}O_{33}$ and (b) D-$Mo_xNb_{12}W_{1-x}O_{33}$.

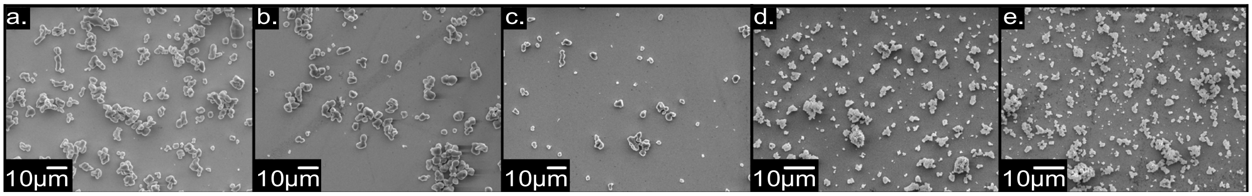

Figure S3. SEM images of (a) $Nb_{12}WO_{33}$, (b) $Mo_{0.25}Nb_{12}W_{0.75}O_{33}$, (c) $Mo_{0.5}Nb_{12}W_{0.5}O_{33}$, (d) $Mo_{0.75}Nb_{12}W_{0.25}O_{33}$, and (e) $MoNb_{12}WO_{33}$

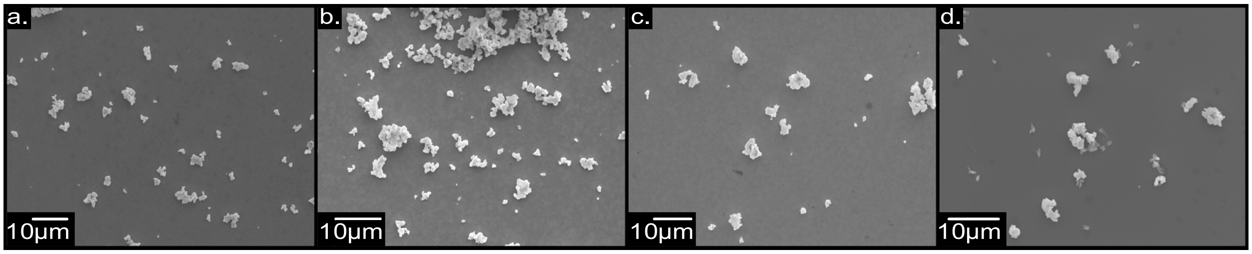

Figure S4. SEM images of (a) D-$Nb_{12}WO_{33}$, (b) D-$Mo_{0.25}Nb_{12}W_{0.75}O_{33}$, (c) $Mo_{0.75}Nb_{12}W_{0.25}O_{33}$, and (d) $MoNb_{12}WO_{33}$

Table S1. Major and minor particle lengths for $Mo_xNb_{12}W_{1-x}O_{33}$.

	$Nb_{12}WO_{33}$	$Mo_{.25}Nb_{12}W_{75}O_{33}$	$Mo_{.5}Nb_{12}W_{.5}O_{33}$	$Mo_{.75}Nb_{12}W_{.25}O_{33}$	$MoNb_{12}WO_{33}$
Major Axis (μm)	3.99 ±1.4 (N=106)	3.61±1.2 (N =93)	3.23±1.1 (N =92)	1.03±0.29 (N =101)	1.02±0.35 (N =100)
Minor Axis (μm)	2.61±0.68 (N =106)	2.68±0.77 (N =93)	2.35±0.72 (N =92)	0.77±0.22 (N =101)	0.78±0.29 (N =100)

Table S2. Major and minor particle lengths for D-$Mo_xNb_{12}W_{1-x}O_{33}$.

	D-$Nb_{12}WO_{33}$	D-$Mo_{.25}Nb_{12}W_{75}O_{33}$	D-$Mo_{.75}Nb_{12}W_{.25}O_{33}$	D-$MoNb_{12}WO_{33}$
Major Axis (μm)	1.54 ± 0.52 $(N = 71)$	1.35 ± 0.44 $(N = 76)$	1.20 ± 0.38 $(N = 42)$	1.13 ± 0.30 $(N = 24)$
Minor Axis (μm)	0.993 ± 0.30 $(N = 71)$	0.940 ± 0.83 $(N = 76)$	0.855 ± 0.27 $(N = 71)$	0.711 ± 0.21 $(N = 24)$

Table S3. Raman mode assignments using phonopy (C2/m; C2h); A_g/B_g are Raman-active (parallel vs crossed).

Spectral window (cm^{-1})	**Dominant motion (A_g/B_g)**	**Intensity**	**Trend with Mo/W and site**	**Rationale for appearance/disappearance**

200–350	Lattice modes: rigid-block tilts, interblock shears (A_g/B_g)	Moderate	Small shifts with mass/force constants; intensity modestly geometry-dependent.	Raman tensor elements are small; geometry and polarization can suppress B_g; convolution/overlap may hide weak lines.
300–500	Framework bends (O–M–O; M = Nb/Mo/W) and tilt-coupled motions (A_g/B_g)	Low	Edge/Corner add extra bending features; Tet keeps a cleaner envelope.	Local octahedral substitutions perturb connectivity → activate/boost otherwise weak bends; Tet has fewer localized bends → fewer narrow lines.
~500–600	Localized framework features tied to Edge/Corner octahedra (B_g-enhanced)	High	Edge/Corner produce new narrow bands; weak/absent for Tet.	Edge/interior octahedra rotate $\partial\alpha/\partial Q$ toward xy/yz → B_g gains; in parallel (A_g-favored) these bands can appear weak or vanish.
~620–680	Collective bends of shear-plane octahedra (A_g/B_g)	High	Tet retains a bifurcated/shouldered band; Edge/Corner shift intensity and sharpen subfeatures.	Mode mixing with nearby stretches varies with site; redistribution of oscillator strength can erase a shoulder or create an extra peak.
700–820	Nb–O–Nb stretches from block edge→interior (A_g/B_g)	Moderate	Edge/Corner concentrate intensity into the mid-frequency manifold; Tet slightly cleaner.	Edge-like Nb–O–Nb motifs are more numerous with Edge/Corner → stronger mid-frequency activity; Tet shares intensity with the high-frequency partner band.
800–900	Block-center Nb–O–Nb stretch that pairs with the tetrahedral band (predominantly A_g)	Moderate	Present and well separated for Tet; Edge/Corner reduce spacing and bleed intensity downward.	In Tet, limited mixing preserves a distinct A_g partner peak; Edge/Corner increase coupling, so intensity is borrowed away, narrowing the high-frequency gap.
900–1060	Tetrahedral M–O symmetric stretch (predominantly A_g)	High	Tet: strong, isolated highest-frequency feature; W lies tens of cm^{-1} above Mo. Edge/Corner: weaker and slightly red-shifted; spacing to Nb–O–Nb shrinks.	Tet provides a localized, stiff M–O(tet) with large parallel-tensor response (A_g). Octahedral environments delocalize/mix the stretch, reducing Raman tensor amplitude and shifting frequency.

Mode Animation 1

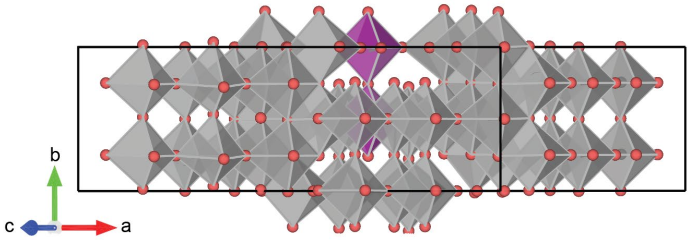

Mode Animation 2

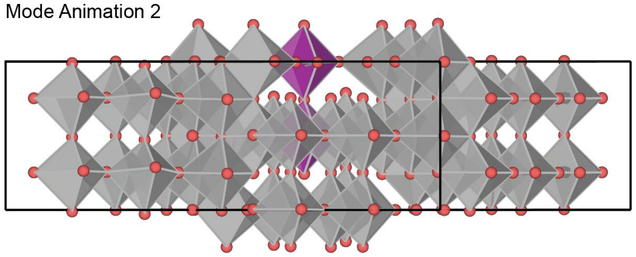

Mode Animation 3

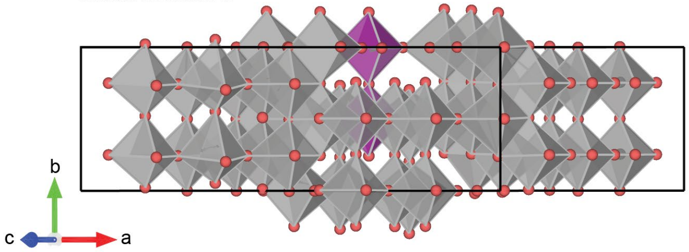

Mode Animation 4

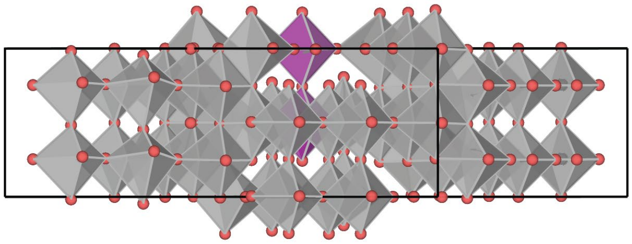

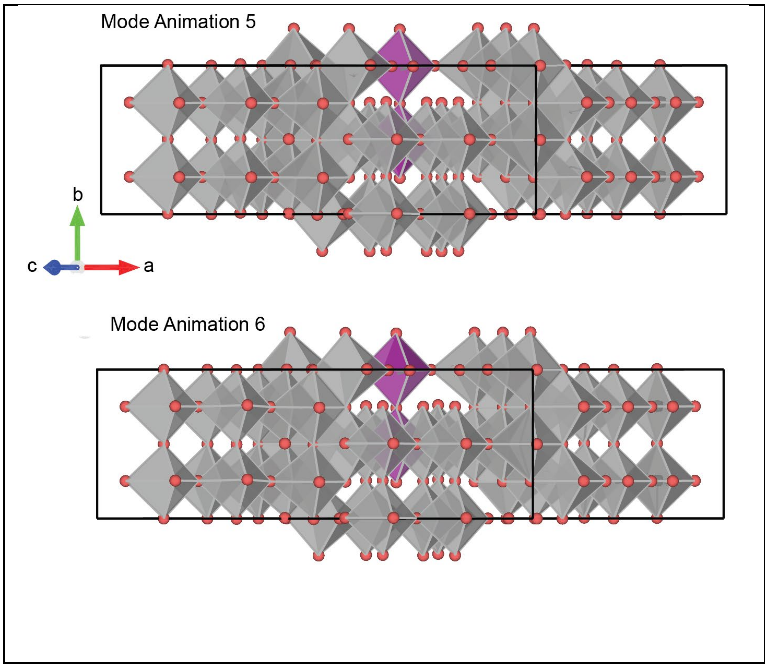

Figure S5. Raman mode animations associated with the spectral feature at 630 cm^{-1}.

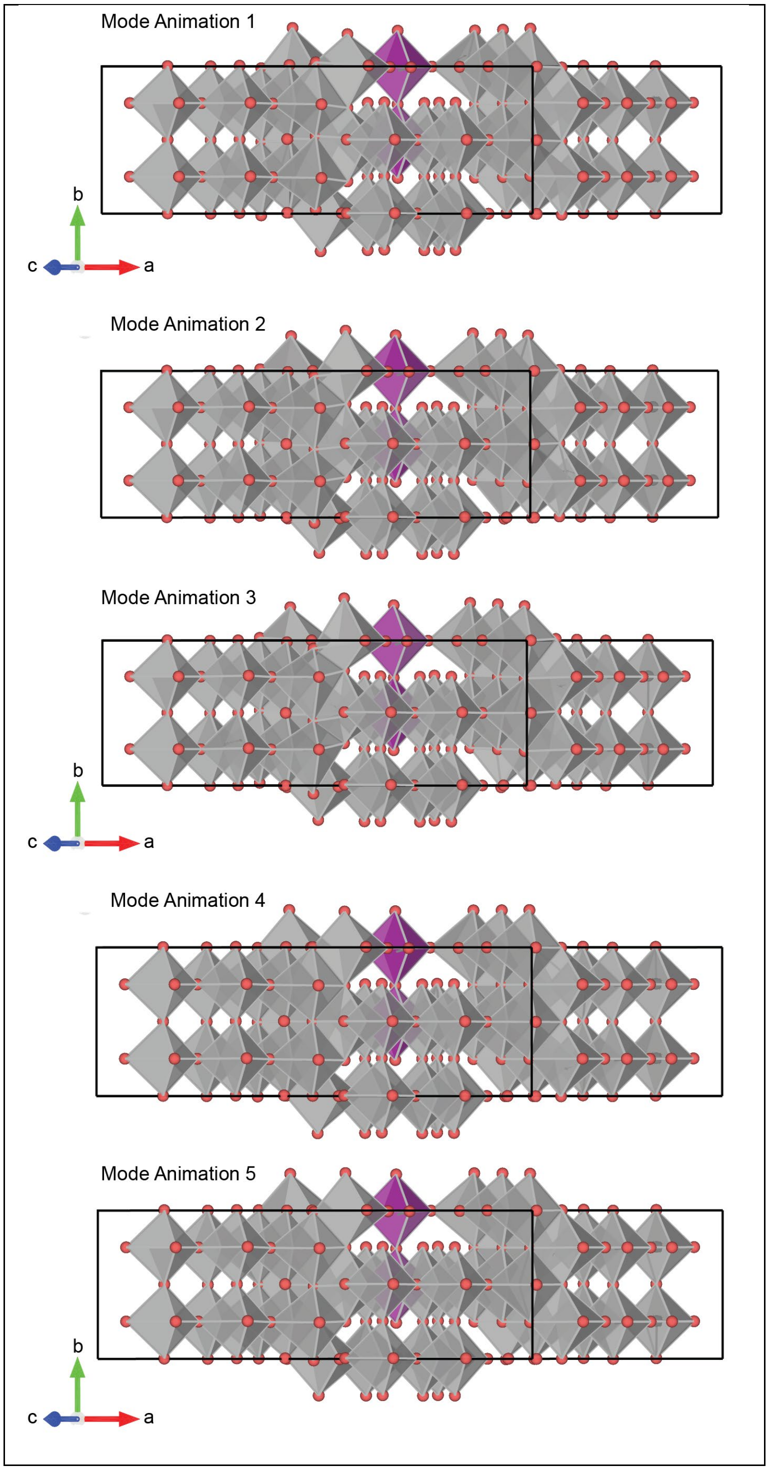

Figure S6. Raman mode animations associated with the spectral feature at 630 cm^{-1}.

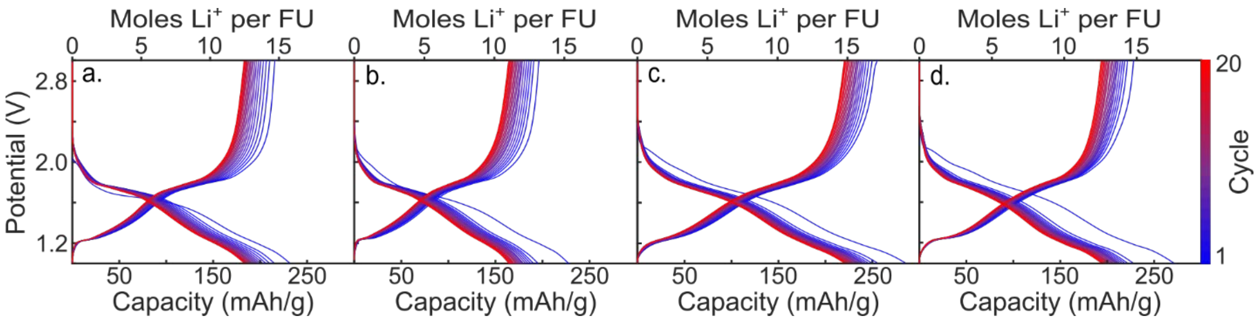

Figure S7. Charge-discharge data for (a) D-Nb$_{12}$WO$_{33}$, (b) D-Mo$_{.25}$Nb$_{12}$W$_{.75}$O$_{33}$, (c) D-Mo$_{.75}$Nb$_{12}$W$_{.25}$O$_{33}$, and (d) D-MoNb$_{12}$O$_{33}$ measured at a C/3 rate.

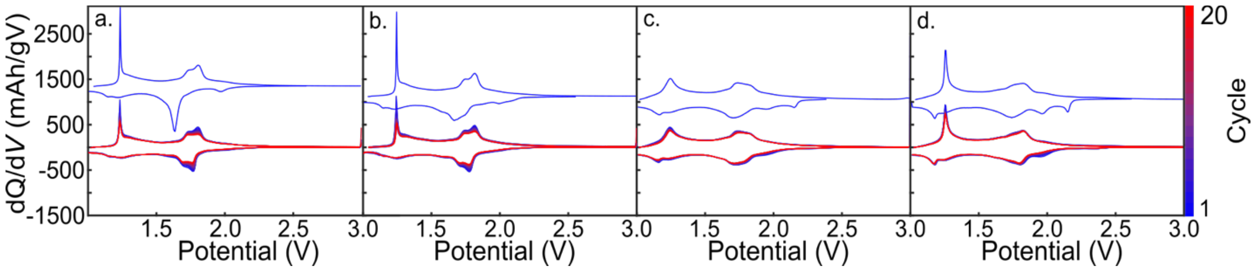

Figure S8. dQ/dV plots for (a) D-Nb$_{12}$WO$_{33}$, (b) D-Mo$_{0.25}$Nb$_{12}$W$_{0.75}$O$_{33}$, (c) D-Mo$_{0.75}$Nb$_{12}$W$_{0.25}$O$_{33}$, and (d) D-MoNb$_{12}$O$_{33}$.

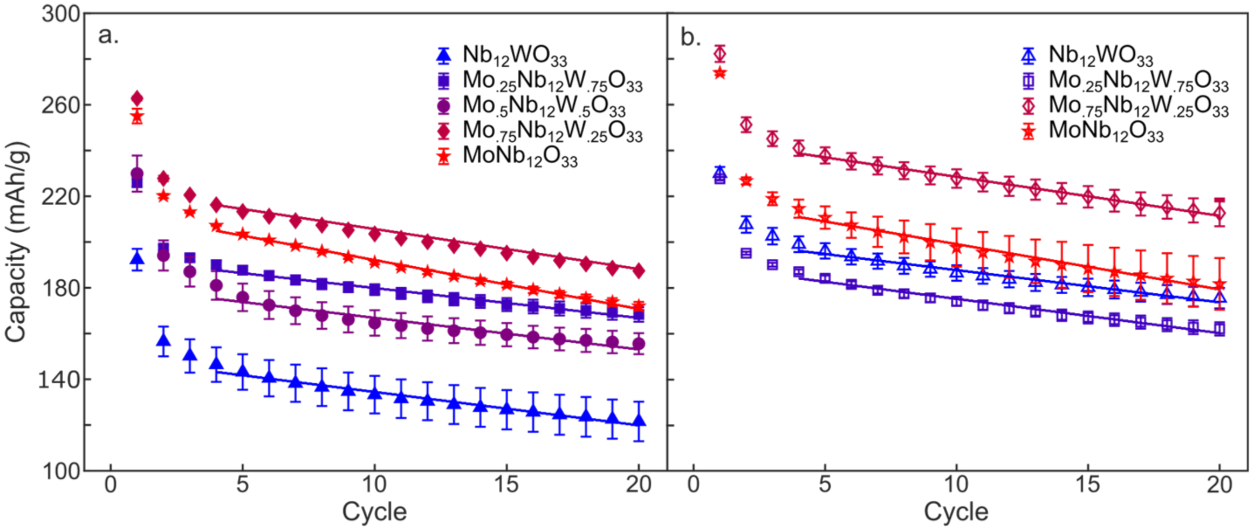

Figure S9. Average discharge capacity versus cycle number (triangles) for (a) $Mo_xNb_{12}W_{1-x}O_{33}$ and (b) D-$Mo_xNb_{12}W_{1-x}O_{33}$. The solid lines in panel (a) represent linear fits to the data for cycles 4-20, yielding slope values of and is –1.60, –1.38, –1.57, –1.82, and –2.24 mAhg^{-1}/cycle for x=0, 0.25, 0.5, 0.75 and 1, respectively. The slope values for panel (b) data are –1.40, –1.49, –1.70, and –1.98 mAhg^{-1}/cycle for x=0, 0.25, 0.75 and 1 respectively.

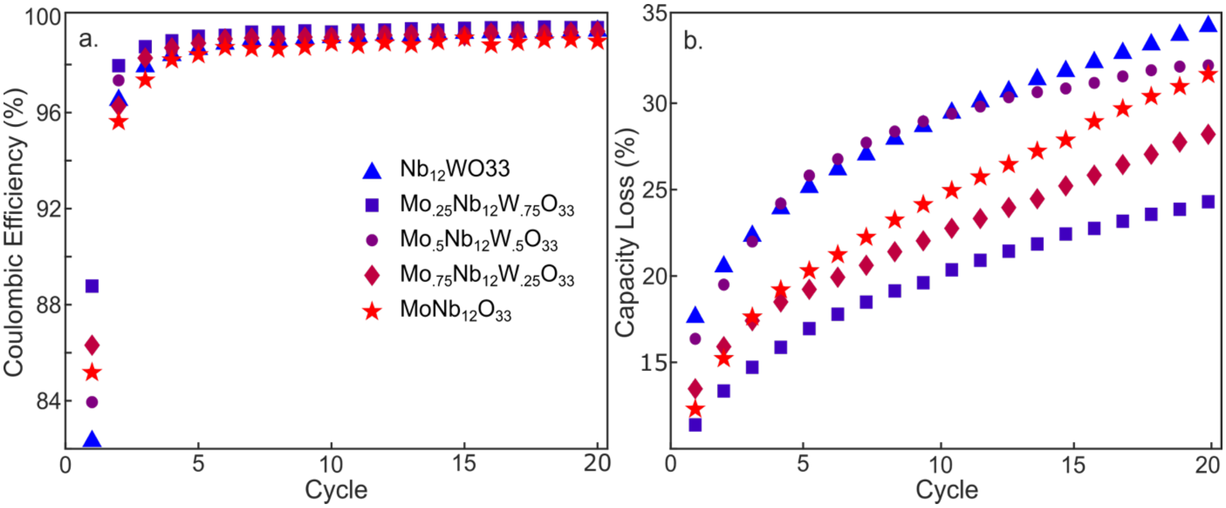

Figure S10. Average (a) coulombic efficiency of $Mo_xNb_{12}W_{1-x}O_{33}$ and (b) percent capacity loss relative to cycle 1.

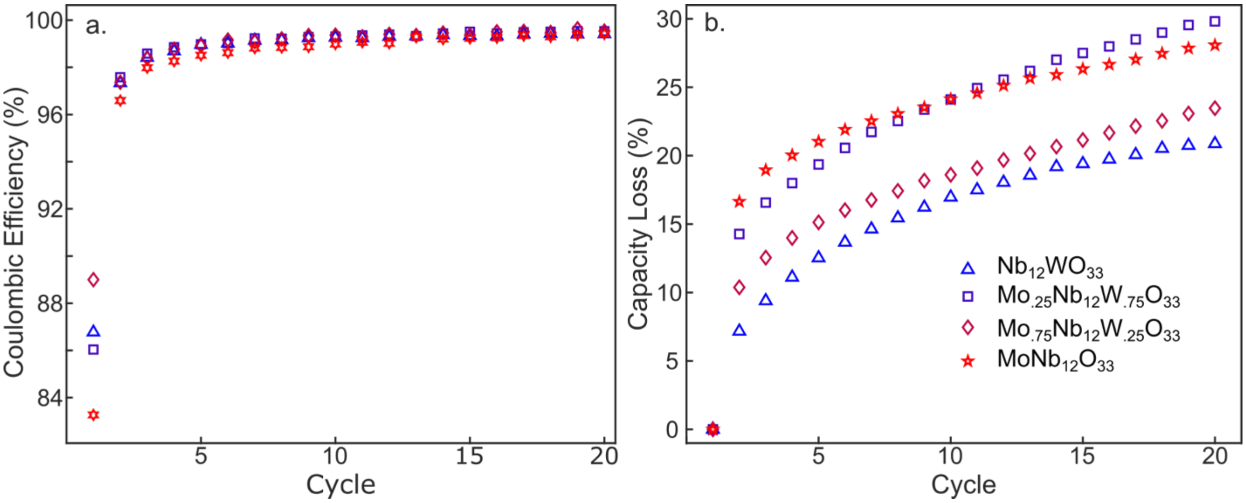

Figure S11. (a) Average coulombic efficiency for D-$Mo_xNb_{12}W_{1-x}O_{33}$. (b) Average capacity loss relative to the first cycle for D-$Mo_xNb_{12}W_{1-x}O_{33}$